Observations of Hot-Star Winds

A. W. Fullerton

Universitäts-Sternwarte München, Scheinerstraße 1, D-81679 München, Germany

1 Introduction

Stellar winds from early-type stars have been studied observationally for more than 120 years, beginning with the detection of peculiar bright lines in visual spectra of a few hot objects by Wolf & Rayet (1867). Beals (1930) first recognized that the emission features of these "Wolf-Rayet stars" (WR stars) were signatures of mass loss, since the observational material available to him showed that some of the line profiles were of the "P Cygni type". This distinctive shape, named because of its prevalence in the spectrum of the famous B2pe hypergiant P Cygni, is also found in the spectra of novae shortly after outburst, i.e., during a time when they are manifestly experiencing explosive mass ejection. On this basis, Beals inferred that WR stars were also losing mass, and concluded that "practically all of the characteristic features of Wolf-Rayet spectra may be explained on the hypothesis that gaseous material from a Wolf-Rayet star is being continually ejected in a radial direction and with high velocity into space".

Thus, more than 60 years ago the modern basis for interpreting spectroscopic emission features in terms of dense, extended, and expanding outflows had already been established. What was not initially clear was that the WR stars and the few objects like P Cygni (which we now call luminous blue variables, or LBVs) are just the tip of the iceberg: they are extreme examples of a phenomenon that is ubiquitous among the early-type stars. Important observations by Wilson (1958) and Underhill (1958) provided hints that mass loss occurs commonly by showing that the emission features of a selection of O-type supergiants and giants could be traced to velocities of 500–1000 kms^{-1}, which are comparable to or in excess of the escape velocity. Nevertheless, during the early and mid-1960s the emphasis in hot-star research was on static atmospheric modelling without the assumption of local thermodynamic equilibrium (LTE), while the field of stellar winds lay fallow.

This situation changed abruptly as a result of technological advances that opened the vacuum ultraviolet region of the spectrum to astronomical observations. The modern era of hot-star wind research began on 1965 October 13 when an Aerobee rocket launched from the White Sands Missile Range in New Mexico briefly carried an ultraviolet spectrograph aloft and returned the first ultraviolet spectra of six early-type stars in Orion (Morton 1967a). As always, a bit of good luck was required to push open a new observational window: Morton (1967a) writes that during the descent,

> the cameras, platform, and gyro had broken free of their mounts and pieces of grating, mirror, and film cassette went flying out of the open end of the rocket skin. Both the calcium fluoride spectrograph camera and a 35-mm camera for photographing the star field were lost, and a 2-day search of the impact area yielded nothing. Fortunately, however, the lithium fluoride film cassette was still attached and was recovered . . . .

Morton's analysis (1967a, 1967b) of these hard-earned data showed that the resonance lines of highly ionized species like Si IV, C IV, and N V exhibited P Cygni profiles. In contrast to the P Cygni profiles that were typically observed in optical spectra of hot stars, velocities well in excess of the escape velocity were directly measured in these ultraviolet data. For the three stars that make up the belt of Orion (from east to west, these are δ, ϵ, and ζ Orionis, with spectral types of O9.5 II, B0 Ia, and O9.7 Ib, respectively), Morton (1967b) estimated mass-loss rates of $\sim 1 \times 10^{-6}$ $M_\odot$ yr^{-1} and concluded that these stars would lose a few per cent of their initial mass during their lifetimes. It at once became clear that garden-variety OB supergiants lose mass continuously at rates that are sufficiently high to affect the course of their evolution.

This result came as a complete surprise at the time. Over the past generation, observational and theoretical efforts to understand the nature and origin of these stellar winds have been a dominant theme of hot-star research. It is a tribute to the success of these efforts that the mass loss carried by these outflows is now recognized to be a fundamental astrophysical process that not only causes individual stars to "evaporate" significantly over their short lifetimes (thereby altering their trajectory through the H-R diagram) but also dumps substantial amounts of energy, momentum, and chemically enriched material into their local galactic environment (thereby influencing the dynamics of the interstellar medium and subsequent formation of stars). Excellent introductions to hot stars and their winds include Kudritzki (1988), Kudritzki & Hummer (1990), and Owocki (1990), while Maeder & Conti (1994) provide an overview of the role these objects play in the evolution of galaxies.

The aim of these lectures is to provide an introduction to the most useful observational signatures of the stellar winds of early-type stars. The goal is to provide an appreciation of the physical ingredients and assumptions that are required to obtain estimates of the physical parameters of the winds from these diagnostics, in particular the mass-loss rate, $\dot{M}$, and the asymptotic (terminal) velocity of the wind at large distances from the star, v_∞. The problems associated with each type of diagnostic are also discussed, in order to assess the reliability of the parameters determined from them. The emphasis is on Population I objects, especially O stars and BA supergiants, though many of the same diagnostics can be applied to related (but more complicated) objects like WR stars and LBVs, and hot Population II objects

like the central stars of planetary nebulae.

2 Tracers of Stellar Winds

The observable manifestations of stellar winds are all attributable to the fact that rapidly expanding material surrounds that star, and this material constitutes an excess with respect to an otherwise identical star whose photosphere manages to maintain strict hydrostatic equilibrium. The fundamental equation that connects the hydrodynamic variables of the outflow is the equation of mass continuity. For a homogeneous, steady, spherically symmetric wind, it reduces to a formula for the mass-loss rate:

$$\dot{M} \;=\; 4\,\pi\,r^2\,v(r)\,\rho(r) \quad . \tag{1}$$

Rearrangement of (1) shows that at large distances in the wind, where $v(r) \approx v_\infty$, the density decreases only as r^{-2}, which is much slower than the exponential decrease characteristic of the hydrostatic layers of the photosphere. It is the presence and motion of this excess circumstellar material that ultimately permit the outflow to be observed.

Even though they represent large density excesses with respect to hydrostatic atmospheres, the stellar winds of early-type stars consist of very rarefied gas. For example, if we insert parameters typical of an O supergiant into (1), we find that at a height of 1 $R_\star$, the density of the wind is approximately 5×10^{-15} g cm^{-3}, which is more than three orders of magnitude smaller than photospheric densities. Thus, stellar winds are environments where radiative processes dominate over collisional processes in determining level populations; i.e., they are very far from being in LTE.

The tracers of this material can be grouped into two main categories: spectroscopic or line diagnostics; and photometric or continuum diagnostics. Signatures can be found in all wavelength regions, from the radio and infrared (IR) through the optical and ultraviolet (UV) to X-rays and possibly even γ-rays (see, e.g., Chen et al. 1996). The emission of these extremely energetic photons is believed to result from time-dependent processes in the wind and not from the steady-state outflow itself, and will not be discussed in detail here.

3 Spectroscopic Diagnostics

Quite generally, spectroscopic observations of absorption or emission lines formed in the atmospheres of stars can be characterized by their positions (i.e., their radial velocities), their strength (i.e., their equivalent widths), and their overall morphology (i.e., the shape of their flux profiles). Each of these measurable quantities can be used to obtain information about the presence of stellar winds.

For example, systematic trends showing decreasing blue shifts for lines formed at increasing photospheric depth – the so-called Balmer progressions or velocity-excitation relations – are frequently used as stellar wind indicators, because they imply the presence of a deep-seated velocity field that increases outwards and presumably drives mass loss (Hutchings 1979; Kaufer et al. 1997). Systematic trends in the strength of photospheric lines as a function of luminosity may also provide evidence for an outward accelerating velocity field, particularly if they are accompanied by asymmetric line profiles with extended blue wings. The velocity gradient is the essential physical ingredient here, because it systematically shifts the absorption profile of the particular ion to smaller wavelengths at greater atmospheric heights, with the result that more atoms can participate in the formation of the flux profile (hence the increase in the equivalent width of the line) and the flux profile has an extended blue wing (since some of the profile is actually formed at blue-shifted velocities). Mihalas (1979) and Kudritzki (1992) provide useful discussions of this phenomenon, which is nicely illustrated for a sequence of B1 supergiants by Massa et al. (1992).

However, the dominant spectroscopic signatures of stellar winds are the profiles associated with lines that are formed in the rapidly expanding part of the wind. Many profile morphologies are recognized as being formed in outflowing material. These shapes were classified qualitatively by Beals (1950), and although his scheme is not much used these days, it still provides a useful introduction to the phenomenology associated with stellar wind profiles. Beals recognized eight classes of wind profiles.

Type I: This is the classic P Cygni profile, which consists of a blue-shifted absorption "trough" and a red-shifted emission "lobe". The origin of this shape is discussed in §3.2.

Type II: These profiles are composed of a Type I profile superimposed on a broad, shallow absorption line, typically one from the Balmer series of hydrogen.

Type III: This morphology consists of red- and blue-shifted emission peaks and a central reversal. It occurs rarely in OB stars, and then only in some lines of rapid rotators. Although its origin is not completely understood, this shape is due to a combination of the velocity fields associated with radial outflow and rapid stellar rotation; see, e.g., the profiles calculated by Petrenz & Puls (1996), in particular their Figs. 12 and 14.

Type IV: These profiles are similar to those of Type I, except they also have one or more extra absorption components in the absorption trough or near the center of the emission lobe.

Type V: These "pure emission" profiles are approximately symmetric about the systemic velocity of the star and do not exhibit the absorption trough characteristic of P Cygni profiles. The spectra of WR stars are dominated by such emission lines, which can also be found in spectra of OB supergiants.

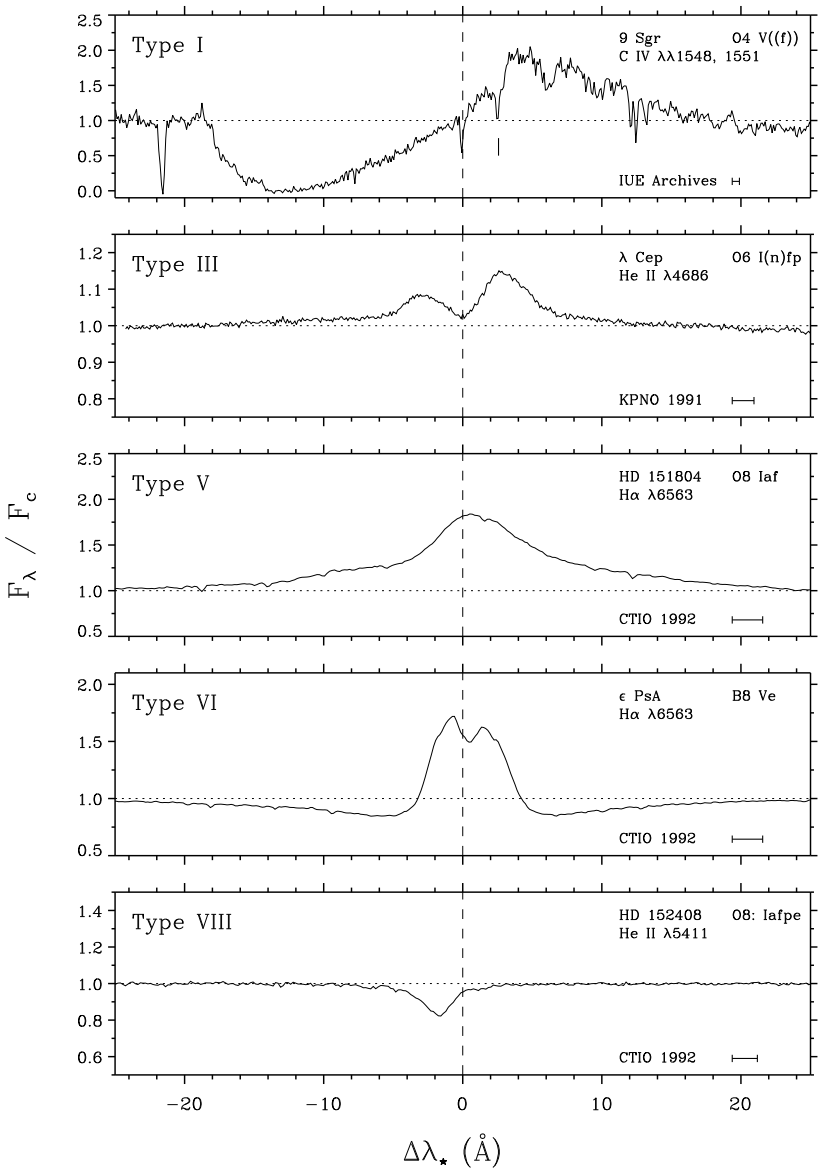

Fig. 1. A selection of line profile morphologies attributed to stellar winds, with classifications according to the scheme of Beals (1950). The wavelength interval corresponding to a velocity of 100 km s^{-1} is indicated by a horizontal bar in the lower right-hand corner, and the position of the red component of the C IV doublet is marked by a vertical line (and the sharp interstellar component).

Table 1. Selected atlases of stellar wind profiles

Reference	Wavelength	Source	Objects
Walborn et al. (1985)	1200–1900 Å	IUE/SWP	O stars
Snow et al. (1994)	1200–3000 Å	IUE	O3–F8 stars
Walborn et al. (1995)	1200–1900 Å	IUE/SWP	B stars
Walborn & Bohlin (1996)	1000–1200 Å	Copernicus	OB stars
Stahl et al. (1993)	4050–9050 Å	FLASH	P Cygni
Hanson et al. (1996)	K band (2μ)	various	OB stars

Type VI**:** This strange morphology consists of a central emission feature that is superimposed on a broad underlying absorption line. The emission is frequently double peaked. These profiles are most commonly associated with Be stars, and consequently a complicated structure of a rotating, expanding stellar wind is implicated in their formation.

Type VII**:** Beals (1950) describes this morphology as "simply an ordinary undisplaced absorption line such as may appear in any normal star ...", and as such it perhaps best serves as a reminder that not all the lines in the spectrum of an early-type star are formed in the moving envelope.

Type VIII**:** Lines of this type are blue-shifted absorption features, which Beals (1950) thought of as Type I profiles without the emission lobe. The displaced absorption is frequently asymmetric, with a shallower blue wing that is presumably due to the velocity gradient through its region of formation.

Part of this classification scheme is illustrated in Fig. 1, which shows normalized flux profiles as a function of wavelength offset from the rest velocity (corrected for the systemic velocity of the star). Examples of stellar wind profiles can be found throughout the observable regions of the spectrum, from the UV through the optical to the IR. Table 1 lists several atlases that illustrate the rich variety of wind profile morphologies implied by the Beals classification scheme.

3.1 Scattering Versus ρ^2 Formation Processes

The resonance lines of singly or multiply ionized species that are typically found in the UV region of the spectra of early-type stars are superb tracers of the rarefied material found in stellar winds. By definition, resonance lines are the lowest energy transitions that arise from the ground state. Consequently, these transitions have very short lifetimes, which in turn means that they occur frequently and are intrinsically strong. In particular, the lifetime

of a resonance transition is usually much shorter than the time required for radiative excitations or collisions, especially in environments characterized by dilute radiation fields and low particle densities. Thus, when an electron is promoted from the ground state to the first permitted level by absorption of a stellar continuum photon of the appropriate frequency, it will de-excite very rapidly and a resonance line photon will be emitted. The net result of such an interaction is that the incoming, almost radially directed, stellar photon will be scattered into some different direction, thereby imparting radial momentum to the ion without changing the population of the ground state. Consequently, in low-density gases the degree of excitation of an ionic species tends to be very low and there is always a large pool of electrons sitting in the ground state that are capable of scattering radiation.

These factors make resonance lines strong and easily detectable throughout the entire volume of the wind where the ion exists. Since these lines are formed by scattering of continuum photons, their strength depends linearly on ρ, the density of matter, and also on the mean intensity of the dilute radiation field from the star. The resonance lines that are important depend on the ionization balance of the wind, which is largely determined by the radiation field. For O- and early B-type stars, they include multiply ionized species like C IV, N V, and Si IV; for mid- to late B- and early A-type supergiants the resonance lines of singly ionized C, Mg, Al, Si, and Fe are important.

However, as Fig. 1 indicates, wind profiles can also be found in the excited (i.e., non-resonance) transitions that are typically located in the optical and infrared regions of early-type spectra, especially those arising from H, He I and He II. They are usually the result of recombinations from a higher ionization stage, which are followed by radiative de-excitations that create photons. These transitions are intrinsically weaker than resonance lines; furthermore, since the process of recombination requires the interaction of an electron and an ion, they are sensitive to ρ^2. Consequently, and in contrast to resonance lines, excited transitions are only sensitive diagnostics of the densest regions of the wind, which are usually the parts closest to the star. An important exception occurs if a large population accrues in the lower level of an optical transition for some reason (e.g., the level is metastable or susceptible to non-LTE/dilution effects), in which case the transitions arising from it behave a bit like resonance lines. The He I λ5876 triplet in the "yellow" region of the visible spectrum is an example of such a transition.

3.2 Dissecting the P Cygni Profile

Before we can determine what information about the stellar wind is contained in line profiles like those shown in Fig. 1, we need to understand how these profiles are formed. The P Cygni profiles (Beals Type I) of resonance lines provide the key to understanding these morphologies.

The basic picture is illustrated schematically in Fig. 2(a), which shows a plane through a smooth, spherically symmetric stellar wind. Four ions (la-

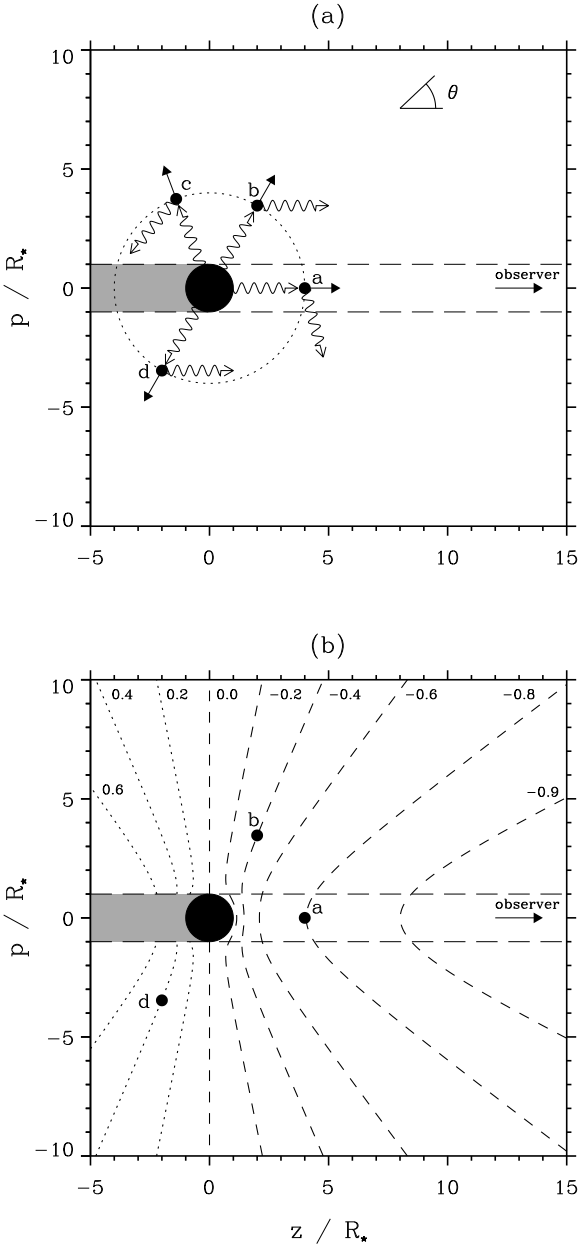

Fig. 2. (a) Schematic diagram of the scattering process. (b) The isovelocity contours associated with the velocity field of a smooth, spherically symmetric stellar wind.

belled a–d) are shown, all of which are located at the same radial distance from the star and therefore experience the same expansion velocity (which is indicated by short, radially directed vectors). Ions at larger (smaller) radii than those illustrated will be moving faster (slower), since the velocity field of a smooth wind increases monotonically outwards. Stellar continuum photons are injected continuously into the wind from the star along paths that are nearly radial. If their wavelength matches the Doppler-shifted wavelength of the resonance line transition associated with ions a–d, then the photon can interact radiatively; since the wind material is moving away from the star, this means that the wavelength of the continuum photons must be blueward of the rest wavelength of the resonance line. An important consequence of this "tuning" is that if a continuum photon can interact with the resonance transitions at some particular radius, it cannot interact with ions at larger or smaller radii, because their Doppler shifts will be greater or smaller, respectively. Consequently, at larger or smaller radii the wind is *transparent* to the photons that can be scattered in the resonance lines of the ions indicated in Fig. 2.

As described above, the net result of this interaction for a resonance line is that the incoming photon is scattered into some different direction. These scatterings have two consequences for a distant observer (who is arbitrarily situated in the z-direction in Fig. 2): (1) photons that were destined to be recorded by the observer can be removed from the line of sight, as in the case of the scattering illustrated for ion "a"; and (2) photons that were not originally heading in his/her direction can be redirected into his/her telescope, as illustrated for ions "b" (where the photon is forward-scattered into the direction of the observer from an ion in the hemisphere approaching the observer) and "d" (where the photon is back-scattered from an ion in the receding hemisphere). Since the observer's direction subtends a very small fraction of the $4\,\pi$ steradians surrounding the star, there is a good chance that an originally unobservable photon will be scattered into a new direction that is also unobservable, as illustrated for ion "c". Some photons will even be back-scattered directly to the stellar surface where they will be reabsorbed by the photosphere.

We can be more specific about the distribution of the scattered photons as a function of position in the flux profile seen by the distant observer. This position may be given in terms of wavelength, frequency, or "radial velocity"; we will usually use the velocity coordinate, but will refer to it as "line-of-sight" velocity, ($V_{\rm LOS}$), in order to avoid confusion with the radial component of the velocity field associated with the stellar wind. The $V_{\rm LOS}$ of a scattered photon depends on the Doppler shift due to wind expansion of the ion that it interacted with and the projection of this displacement onto the observer's line of sight, i.e., the cosine of the angle θ between the velocity vectors and the z-axis indicated in Fig. 2(a). Contours of equal $V_{\rm LOS}$ for the velocity field of a typical expanding stellar wind are shown in Fig. 2(b), where they are

labelled in units of v_∞ with positive velocities denoting recession. Of course, these contours in the equatorial plane are actually surfaces in 3D space; they are sometimes called "common direction" (CD) surfaces since they require the specification of the direction of an observer (see, e.g., Rybicki & Hummer 1978).

The isovelocity contours permit the redistribution of continuum photons to be mapped to positions in the observed line profile, which can be conveniently divided into an absorption part and an emission part. This mapping is illustrated in Fig. 3 for a line of moderate strength (panel a) and a strong line (panel b). Three regions of the wind contribute to the profile:

1. Material in the column projected against the disk of the star removes continuum photons from the line of sight at blue-shifted velocities that range from 0 to the maximum expansion velocity where the ion still exists (which is frequently v_∞), thereby producing the blue-shifted absorption trough. Ion "a" provides an example of the removal of a photon at $V_{\rm LOS} = -0.8\,v_\infty$).
2. Material at other places in the approaching hemisphere adds photons at blue-shifted velocities (e.g., ion "b": $V_{\rm LOS} = -0.4\,v_\infty$) by forward-scattering, which collectively produce the blue-shifted emission shown in the middle panels of Fig. 3. In contrast to the absorption trough, the emission at a particular $V_{\rm LOS}$ includes contributions from many different radii that will in general sample a wide range of densities, temperatures, and ionization equilibria.
3. Material in the receding hemisphere adds back-scattered photons at red-shifted velocities (e.g., ion "d": $V_{\rm LOS} = +0.4\,v_\infty$) to the emission profile. The emission profile is not symmetric about $V_{\rm LOS} = 0$ because back-scattered photons originating in the shaded "occultation region" are re-absorbed by the stellar core before they can reach the observer. The differences between the blue- and red-shifted emission are especially pronounced for winds that expand more slowly, since in these cases the star subtends a larger solid angle at radii where the density is still high enough for many scattering interactions to occur.

The bottom panel shows how a P Cygni profile results from adding the absorption and emission contributions from these regions to produce the characteristic morphology of a blue-shifted absorption trough and a red-shifted emission lobe.

The comparison between moderate and strong scattering lines in Fig. 3 is also instructive. The upper panels show that for a line of sufficient intrinsic strength, all the continuum photons can be scattered from the observer's line of sight, whereas a weak line in the same wind (i.e., same ionization and density structure) will not completely extinguish the continuum light directed toward the observer. By the same token, the strong line will scatter more photons towards the observer, so that its emission component (middle panel) is stronger at all velocities. This is a reflection of the fact that scattering is a

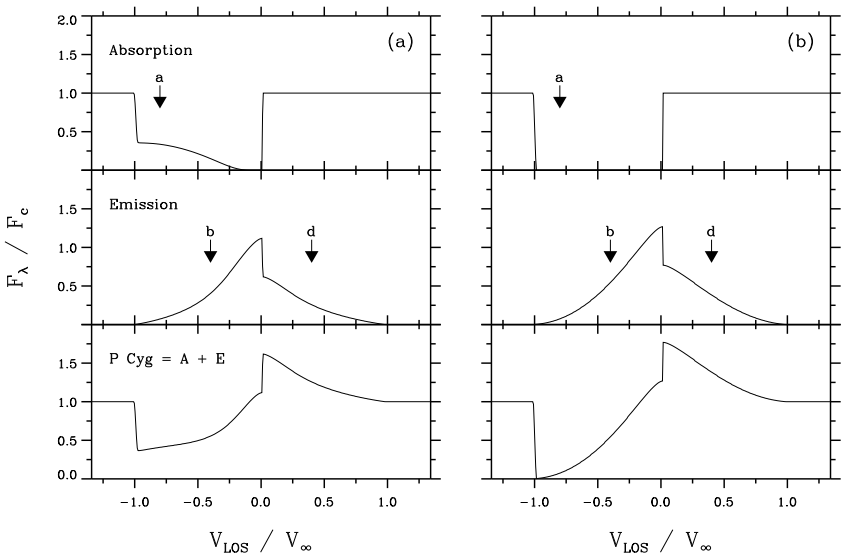

Fig. 3. Schematic diagram showing the formation of a P Cygni profile of a UV resonance line for the case of (a) a moderately strong line; and (b) a strong line.

conservative process: since photons are not created or destroyed in the wind (though some are lost through back-scattering to the photosphere), and since the absorption component of a strong line removes more photons from the observer's line of sight compared to a weak line, more photons must be forward- and back-scattered towards the observer.[1] Thus, despite the total extinction of the continuum source by the cylinder of material projected against the disk of the star, the P Cygni absorption trough of a strong line formed in a smooth, spherically symmetric wind never exhibits extended regions of zero flux. If the ion responsible for the strong resonance line exists throughout the wind, then the only place where its absorption trough will have zero flux is at $V_{\rm LOS} = v_\infty$, since forward-scattering from material anywhere else in the approaching hemisphere will necessarily be seen at smaller line-of-sight velocities. Put another way, the isovelocity contours collapse to a point for $V_{\rm LOS} = \pm v_\infty$, and the positive case is not observable due to occultation by the star. Hence, for monotonically expanding winds, the maximum velocity seen at the blue-edge of the absorption trough of a strong line is a good diagnostic of v_∞.

P Cygni profiles are formed when scattering dominates the transfer of ra-

[1] This argument breaks down after all photons have been removed from the absorption trough, at which point the strength of the emission lobe also saturates.

diation through the wind. If instead photons are created in the wind through radiative or collisional ("ρ^2") processes, the absorption component tends to be filled in by locally produced photons. Similarly, the emission component can become very strong, since the number of photons that emerge from the wind is not simply a reflection of the number of stellar continuum photons initially injected. Unless there is some additional factor associated with the physics of the transition in question (e.g., the lower level is overpopulated for some reason), "pure emission" profiles are formed in these cases. Although the atomic processes responsible for these spectral features are more complicated than resonance line scattering, the mapping between isovelocity contours and position in the profile remains the same. Of course, more complicated velocity fields (e.g., coupling between rotation and expansion) or geometries (e.g., disks) will change the shape of the contours, and the interplay between the velocity field, density distribution, and ionization balance in the wind are ultimately responsible for the variety of wind profile morphologies catalogued by Beals.

Although P Cygni profiles are unambiguous signatures of outflow, the same is not true of pure emission features. For example, there are a number of narrow emission lines in the spectra of O stars (see, e.g., Morrell et al. 1991 or Underhill 1995a,b for recent discussions), most of which are formed by two-electron processes ("dielectronic recombinations") in deep layers of the atmosphere. The most famous of these are the N III $\lambda\lambda$4634, 4640, 4641 lines, whose formation in static, plane parallel atmospheres was first explained by Mihalas & Hummer (1973). Although the strength of these features often suggests that they are partially formed in the low-velocity region of the stellar wind, they should be distinguished from the very broad stellar wind profiles typical of Beals Type III or V.

3.3 Calculation of Line Profiles Formed in Stellar Winds

The preceding discussion of the P Cygni profile also illuminates many aspects of the problem of computing line profiles formed in a stellar wind. In general, this is a formidable task; but, as Castor (1970) realized, it can be handled very effectively by combining the formalism of escape probabilities (see, e.g., §3.2 of Hubeny's lectures in this volume) with the Sobolev approximation. What follows is a sketch of this approach as it applies to smooth, spherically symmetric, monotonically expanding winds. For rigorous discussions of this elegant technique, see Castor (1970), Rybicki & Hummer (1978), Rybicki (1984), or Mihalas (1978; Chapter 14). Although the escape-probability formalism is at present the most widely used, alternative approaches exist: see, e.g., Lucy (1971).

The equation of radiative transfer in the observer's frame for spherically symmetric geometry is given, e.g., by (27) in Hubeny's lectures.[2] It can be

[2] For convenience, results presented by Hubeny will be referred to by their equation

reformulated in the Cartesian "p–z" geometry illustrated in Fig. 2 as an ordinary differential equation for rays specified by their impact parameter p:

$$\frac{\mathrm{d}I_\nu(z;p)}{\mathrm{d}z} = k_\nu\,(z;p)\,[S_\nu\,(z;p) - I_\nu\,(z;p)] \tag{2}$$

where r, $z = r\,\mu$ and $p = r\,\sqrt{1-\mu^2}$ are measured in units of $R_\star$ and $\mu \equiv \cos\theta$ is the cosine of the angle between a point in the wind and the direction to the observer, as indicated in Fig. 2(a); k_ν is the absorption coefficient; and where "complete redistribution" has been assumed (see §3.1 of Hubeny's lectures). This reformulation is a great simplification, and allows the "formal solution" to be written down immediately. If $I_\nu^\star$ is the continuum intensity of the star at frequency ν and $z_\star = \sqrt{1-p^2}$ denotes the z-coordinate associated with the stellar surface for $p \le 1$, then the formal solution is:

$$I_\nu(p) = \begin{cases} \int_{z'=-\infty}^{z'=\infty} S_\nu(z')\,\mathrm{e}^{-\tau_\nu(z')}\,\mathrm{d}\tau_\nu(z') & \text{for } p \ge 1 \\ \int_{z'=z_\star}^{z'=\infty} S_\nu(z')\,\mathrm{e}^{-\tau_\nu(z')}\,\mathrm{d}\tau_\nu(z') + I_\nu^\star \mathrm{e}^{-\tau_\nu(\infty)} & \text{for } p < 1 \quad , \end{cases} \tag{3}$$

where the optical depth variable is

$$\tau_\nu(z;p) = \int_{z_{\min}}^{z} k_\nu(z';p)\,\mathrm{d}z' \quad , \tag{4}$$

with $z_{\min} = -\infty$ for $p \ge 1$ and $z_{\min} = z_\star$ for $p < 1$. Once $I_\nu(p)$ is known, the flux profile can be calculated directly:

$$F_\nu/F_c = \int_0^\infty [I_\nu(p)/I_\nu^\star]\;2p\,\mathrm{d}p \quad . \tag{5}$$

In the case of line radiation, (3) can be viewed as the mathematical equivalent of Fig. 3. It says that for rays projected against the stellar disk (i.e., $p < 1$) the flux received by a distant observer is made up of a "direct" component that is extinguished by material in front of it (i.e., the absorption trough) and a "diffuse" component (i.e., sources of emission due to forward-scattering). For rays not projected against the stellar disk ($p \ge 1$), only diffuse light is sent to a distant observer. In the case of UV resonance lines, the diffuse light is entirely due to scattering.

Since (3) is a formal solution, the source function and the optical depth for the line of interest need to be known before it can be applied. The level populations for resonance lines are controlled by radiative transitions between only two levels, and so the source function for the two-level atom given by (H82) for the case of "pure scattering" ($\epsilon = 0$) is directly applicable. Hence, $S_\nu = \overline{J}$, where $\overline{J}$ is the frequency-averaged mean intensity of line radiation defined by (H81). Schematically, the mean intensity can be viewed as a competition between the number of continuum photons that arrive at location

numbers in his lectures preceded by "H": e.g., (H27).

r versus the number of line photons that escape from the same location, so that

$$\overline{J}(r) = \frac{\text{probability that a stellar continuum photon penetrates to } r}{\text{probability that a line photon escapes from } r} \quad . \quad (6)$$

These quantities are related to the angle- and frequency-averaged escape probabilities defined by (H88), which in turn depend fundamentally on the optical depth variable for different directions μ at location r in the wind. Consequently, the computation of a line profile pivots on the computation of τ_ν, after which the calculation can be charted as $\tau_\nu \rightarrow$ escape probabilities $\rightarrow$ $\overline{J} \rightarrow S_\nu \rightarrow I_\nu(p) \rightarrow F_\nu$.

Unfortunately, the calculation of τ_ν for arbitrarily moving media is complicated by the frequency dependence of the absorption coefficient, k_ν. In static atmospheres, k_ν is often written as the product of a spatial part and a normalized absorption profile that accounts for the frequency dependence (and is generally assumed to be constant);

$$k_\nu = k_0(r) \times \varphi(\Delta\nu) \ , \quad (7)$$

where $\int_{-\infty}^{+\infty} \varphi(\Delta\nu)\,\mathrm{d}\nu = 1$ and $\Delta\nu = \nu - \nu_0$ for a line with rest frequency ν_0. This separation is not strictly valid in a moving atmosphere, because ν is itself a function of r owing to the bulk motion of the fluid, but the functional form can be recovered by allowing explicitly for the Doppler shift in frequency, which can be accomplished by redefining $\Delta\nu = \nu - \nu_0 + [\nu_0 \cos\psi\, v(r)]/c$, where ψ is the angle between the radial direction and the direction of scattering, so that $\cos\psi\, v(r)$ is the projection of the expansion velocity onto the new direction of flight. Although this simple redefinition allows us to retain the form of (7), it also shows that in a moving medium, $k_\nu \equiv k_\nu\,(r, v, \psi)$, i.e., that frequency and spatial variables are intertwined, so that many different combinations of positions and frequency contribute to a particular frequency in the observer's frame; recall, e.g., the isovelocity contours illustrated in Fig. 2(b).

However, in the presence of sufficiently large velocity gradients, the "tuning" required for a photon to excite a line transition localizes the material that is capable of absorbing it, and this breaks the coupling between frequency and spatial variables. This localization is the essence of the Sobolev approximation, which is sometimes called the "large velocity gradient" or "supersonic" approximation. Fig. 4(a) illustrates the Sobolev approximation in a schematic way for the frame of reference that is moving with the mean flow of the expanding wind. The star is receding with respect to this "comoving frame", and the thick solid line shows the systematic redshift of a photon emitted with wavelength $\lambda_\star$ at the stellar surface as a function of radius. Consider a bound-bound transition with rest wavelength λ_0 in the spectrum of an ion, and suppose for the moment that the absorption profile $\varphi(\Delta\lambda)$ of this transition is a delta function. The photon $\lambda_\star$ travels *unimpeded*

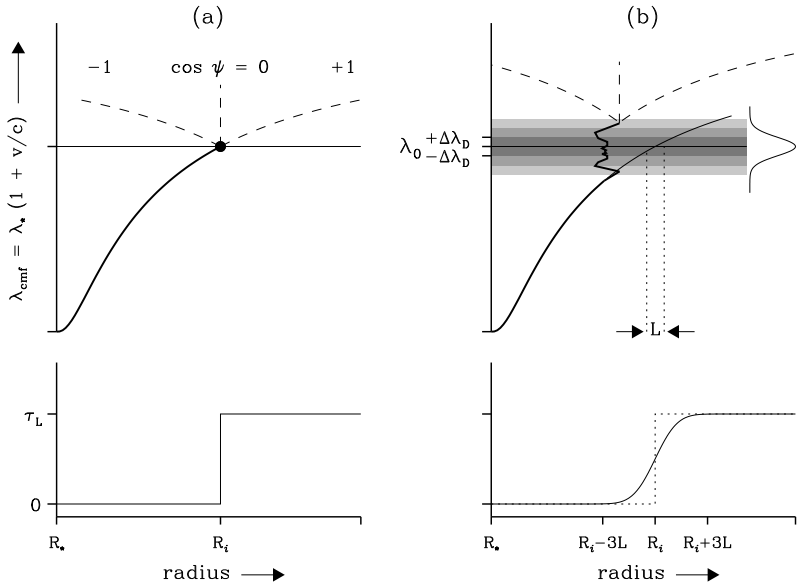

Fig. 4. Schematic illustration of the Sobolev approximation (after Owocki 1990) and the distribution of Sobolev optical depth for (a) an infinitely thin transition centered on λ_0; (b) a transition with a Gaussian profile characterized by a 1-sigma dispersion of $\Delta\lambda_D$.

through the material of the stellar wind until its wavelength in the comoving frame matches λ_0, whereupon it may be absorbed by the line transition and re-emitted in some other direction. Three possible scatterings are indicated in the upper panel of Fig. 4(a), which correspond to forward-scattering ($\cos\psi = 1$; i.e., the photon continues along its original course); sideways-scattering ($\cos\psi = 0$); and back-scattering towards the star ($\cos\psi = -1$).

The key point is that since the wind is an expanding medium, the material in *any* direction is receding from the scattering site, just as all galaxies recede from one another in the case of the expanding universe. Thus, irrespective of the scattering angle, the wavelength of the redirected photon in the comoving frame must be redshifted, which means it cannot interact again with a transition of wavelength λ_0 and is free to travel through the wind along its new trajectory. As a result, the processing of stellar continuum photons through a bound-bound transition is localized to a single radius, R_i, which is determined by $\lambda_\star$, and the variation of optical depth with radius is the step-function shown in the lower panel of Fig. 4(a). For this simplified case, the solution of the equation of radiation transfer reduces to determining the fraction of incident photons that are scattered into the different directions ψ.

In practice, the absorption profile of a transition is never a delta function, but has a finite width $\Delta\lambda$ associated with it; e.g., the absorption profile is dominated by thermal Doppler broadening in the low-density environments typical of hot-star winds, so that φ is a Gaussian characterized by a root-mean-square dispersion parameter (sigma) of $\Delta\lambda = \Delta\lambda_{\rm D} = v_{\rm th}\lambda_0/c$, where $v_{\rm th}$ is the thermal velocity of the parent ion. This case is illustrated in Fig. 4(b), which shows that after travelling freely through lower regions of the wind (as before) the stellar photon first impinges on the blue wing of the line. The scattered photon will in general be redirected and redistributed in wavelength (frequency), so that it will perform a random walk in space and wavelength that takes it from the weak absorption typical of the blue wing to the strong absorption of the line core. The step size associated with this random walk gets quite small as the photon makes its way towards the line core, but its eventual emergence at the red wing – possibly after many scatterings – is assured because of the overall expansion of the wind.

However, even though the number of scatterings may be very much larger than in the case of the infinitely narrow line, the net result is that a photon is absorbed at the blue wing of the line, emerges after a final scattering in the red wing, and continues its travel in a different direction but without further interactions, exactly as before except that the interaction occurs over a larger range of radii. As shown in the lower panel of Fig. 4(b), the finite width of the line softens the step-function character of the radial distribution of optical depth, but does not affect the essential localization of the interaction region *provided that the velocity gradient is sufficiently steep.* The relevant figure of merit to describe "sufficient steepness" is the Sobolev length, L, which is the distance over which the mean flow speed of the wind increases by $v_{\rm th}$, and can be thought of as the local optical depth scale height. From Fig. 4(b), $\mathrm{d}v/\mathrm{d}r \approx v_{\rm th}/L$ or $L = v_{\rm th}\,(\mathrm{d}v/\mathrm{d}r)^{-1}$. The Sobolev approximation is valid when L is much smaller than the distance over which other hydrodynamical variables (e.g., density) change. The local density scale height, L_ρ, may be estimated from (1):

$$L_\rho \equiv \frac{\rho}{|\mathrm{d}\rho/\mathrm{d}r|} \approx \frac{v}{|\mathrm{d}v/\mathrm{d}r|} \gg \frac{v_{\rm th}}{|\mathrm{d}v/\mathrm{d}r|} = L \quad , \tag{8}$$

since $v_{\rm th} \sim 10$ km s^{-1} while $v \sim 1000$ km s^{-1} for hot-star winds. Thus, the Sobolev approximation is generally excellent, except at small velocities, where $v \sim v_{\rm th}$.

This localization of the radiative transfer enormously simplifies the calculations of τ_ν. Since the radiative transfer occurs over spatial scales that are much smaller than other hydrodynamical scale lengths, the spatial part of absorption coefficient (7) can be taken outside the optical depth integral (4):

$$\tau_\nu(z;p) \overset{\rm SA}{\approx} k_0(r) \int_{z_{\rm min}}^{z} \varphi\left(\nu - \nu_0 + [\nu_0\,\mu\,v(z;\,p)]/c\right) \mathrm{d}z' \quad , \tag{9}$$

which can then be transformed in a straightforward way to an integral over frequency in the comoving frame (i.e., spatial variables can be exchanged for frequency variables). For Gaussian absorption profiles, the integral can be done analytically, which represents a tremendous simplification even compared to static atmospheres. An important result to emerge from these manipulations is the expression for the Sobolev optical depth in the radial direction at a particular radius (or, equivalently, velocity) in the wind. For a transition between a lower level l and an upper level u of an ion, this is

$$\tau_{lu}\ (r) = \left(\frac{\pi\, e^2}{m_e\, c}\right) f_{lu}\, g_l\, \lambda_{lu}\, \left(\frac{n_l}{g_l} - \frac{n_u}{g_u}\right) \left(\frac{\mathrm{d}v}{\mathrm{d}r}\right)^{-1} \quad , \tag{10}$$

where the first terms on the right-hand side denote the strength of the transition in terms of its classical oscillator strength (where all symbols have their usual meanings), λ_{lu} is the rest wavelength of the transition, g_l (n_l) and g_u (n_u) are the statistical weight (number density) of the lower and upper levels, respectively, and $\mathrm{d}v/\mathrm{d}r$ is the local radial gradient of the velocity field.

Once $\tau_\nu(z)$ is known, the calculation of a line profile formed in the stellar wind can proceed according to the plan outlined before. Several computer programs are available for this purpose, the most widely used of which is the efficient "Sobolev with Exact Integration" (SEI) program described by Lamers et al. (1987)[3]. The idea of using the Sobolev approximation to compute the source function, but doing the flux integration "exactly", is due to Hamann (1981) and is in contrast to the previous approach of relying on the step-function behaviour in $\tau_\nu(r)$ inherent to the Sobolev approximation to simplify the integrations as well (e.g., Castor & Lamers 1979). With the SEI approach, it is straightforward to allow for the radiative coupling of the source functions of closely spaced doublets (Olson 1982; see also Lamers et al. 1987), which is of practical importance since most of the UV resonance lines are blended doublets. The SEI formalism is also sufficiently flexible that generalizations to allow for deviations from spherical symmetry (e.g., Bjorkman et al. 1994; Cranmer 1996) or monotonic expansions (e.g., Puls et al. 1993) can be implemented in a simple way. More complicated situations like these can also be treated by using a Monte Carlo approach to radiative transfer: see, e.g., Caroff et al. (1972), Lucy (1983), or Puls et al. (1994).

3.4 UV Resonance Lines

Equation (1) shows that the mass-loss rate for a spherically symmetric wind can be calculated once the radial distribution of velocity and mass density are known. Although quite a lot of information about the "velocity law",

[3] A FORTRAN version of this program can be downloaded from the homepage of Collaborative Computer Project No. 7 (CCP7) on the Analysis of Astronomical Spectra. Its URL is currently `http://star.arm.ac.uk/ccp7/` .

$v(r)$, is encoded in the shape of the P Cygni profile, it is not possible to measure the density distribution directly because the winds of hot stars cannot be spatially resolved at UV wavelengths. On the other hand, the strength of the absorption and emission components constrain the total number of ions of the species responsible for the resonance line that are present in the wind. Consequently, the general strategy for extracting information from the P Cygni profiles of UV resonance lines is to use the integrated line strength from *unsaturated* profiles to constrain the left-hand side of (1), and to rely on the velocity law (which is best determined from strong or saturated lines) for information concerning the radial distribution of the material. The line strength and shape of the velocity law are determined by fitting synthetic profiles computed from parameterized models of the stellar wind to observed line profiles.

Consider the resonance line of ion j of the element with atomic number k. Let the mass of a particle of element k be m_k and its abundance by weight be X_k; then, if $n_{jk}(r)$ and $n_k(r)$ represent the number densities of the ion and its parent element, respectively, it follows that

$$n_{jk}(r) = \frac{n_{jk}(r)}{n_k(r)}\, n_k(r) = q_{jk}(r)\, \frac{X_k}{m_k}\, \rho(r) = \frac{\dot{M}}{4\,\pi}\, \frac{X_k}{m_k}\, \frac{q_{jk}(r)}{v(r)\, r^2} \quad , \tag{11}$$

where $q_{jk}(r) \equiv n_{jk}(r)/n_k(r)$ is the fraction of element k that exists in the ground state of ion j, and where the expression for ρ from (1) has been substituted. We have previously argued that the degree of excitation will be low for ions in a rarefied medium, so that to a good approximation all of the ions k will be in their ground state, which implies that the local Sobolev optical depth in the radial direction given by (10) can be simplified:

$$\tau_{\rm uv}\ \left(v\,(r)\right) = \left(\frac{\pi\, e^2}{m_e\, c}\right)\, f_{lu}\, \lambda_0\, n_{jk}\, \left(\frac{{\rm d}v}{{\rm d}r}\right)^{-1} \quad . \tag{12}$$

The usual approach is to parameterize $\tau_{\rm uv}(v)$ as the product of the integrated optical depth (for ion j of element k), $\mathcal{T}_{jk}$, and a normalized function of velocity, $\mathcal{F}(v;\boldsymbol{\alpha})$ that is defined by adjustable parameters $\boldsymbol{\alpha} = (\alpha_1,\, \alpha_2, \ldots)$, so that

$$\tau_{\rm uv}(v) = \mathcal{T}_{jk}\, \mathcal{F}(v;\boldsymbol{\alpha}) \quad . \tag{13}$$

Lamers et al. (1987) discuss the motivation for some of the more popular functional forms of $\mathcal{F}(v;\boldsymbol{\alpha})$. It is not strictly necessary to assume a functional form for the radial distribution of optical depth, since the absorption trough of unsaturated P Cygni profiles contains sufficient information to determine this empirically (see, e.g., Haser 1995 or Haser et al. 1995 for an alternate, and probably preferable, approach). Nevertheless, with this ansatz, the direct integration of (12) can proceed in terms of known parameters:

$$\int_{v_0}^{v_\infty} \tau_{\rm uv}\ {\rm d}v = \int_{v_0}^{v_\infty} \mathcal{T}_{jk}\, \mathcal{F}(v;\boldsymbol{\alpha})\, {\rm d}v$$

$$= \mathcal{T}_{jk}$$
$$= \left(\frac{\pi\, e^2}{m_e\, c}\right)\, f_{lu}\, \lambda_0 \int_{R_\star}^{\infty} n_{jk}\, \mathrm{d}r$$
$$= \left(\frac{\pi\, e^2}{m_e\, c}\right)\, f_{lu}\, \lambda_0\, \mathcal{N}_{jk} \quad , \tag{14}$$

where $\mathcal{N}_{jk}$ is the column density of ion j of element k between the surface of the star and the observer. The parameters $\boldsymbol{\alpha}$ and $\mathcal{T}_{jk}$ are determined from the fit to the profile, and hence $\mathcal{N}_{jk}$ is also known.

However, in order to fit the profile, the velocity law that describes the distribution of velocity as a function of radius must also be determined. The key parameter (which is traditionally called "β") defines the steepness of the spatial velocity gradient associated with the expansion. There are several versions of the "beta velocity law" that are distinguished by their treatment of the velocity field near the photosphere, but the conventional form is

$$v(r;\, v_0,\, \beta) = v_0 + (v_\infty - v_0)\, \left(1 - \frac{R_\star}{r}\right)^{\beta} \quad , \tag{15}$$

where v_0 is the outflow velocity deep in the wind[4]. Fig. 5 shows the shape of the beta-velocity law for several values of β, and emphasizes that small values of β signify steeper ("faster") gradients. This functional form reflects the necessity of lifting the material out of the gravitational potential well of the star, though the exact value of β depends on details of the mechanism responsible for driving the wind; see, e.g., the lectures by Lamers (this volume) on the theory of line-driven stellar winds. The theory of radiatively driven stellar winds predicts that β should be near 0.8 for O-type stars (Pauldrach et al. 1986).

For a spherically symmetric wind that is smooth and steady, we have already seen that the position of the blue edge of the absorption trough of a strong P Cygni profile is a diagnostic of v_∞. The emission lobe of P Cygni profiles provides information about β; see, e.g., Fig. 6, which shows that both the shape and strength of the emission lobe are sensitive to the velocity gradient for the case of a strong line. Physically, this sensitivity arises from the inverse proportionality between density and velocity implied by (1): for a fixed $\dot{M}$, a "slower" velocity law (larger β) results in higher densities of material at small radii, which enhances the number of photons scattered towards the observer at small values of $V_{\rm LOS}$, all other things being equal. Weaker lines also respond in a similar way to changes in β, but in practice the parameters associated with the velocity field are more difficult to disentangle

[4] Formally, v_0 is the wind velocity at $r = R_\star$, though it is preferable to think of it as the velocity at the sonic point (i.e., the sonic velocity for the ion) since this is where deviations from the hydrostatic density stratification start to become significant.

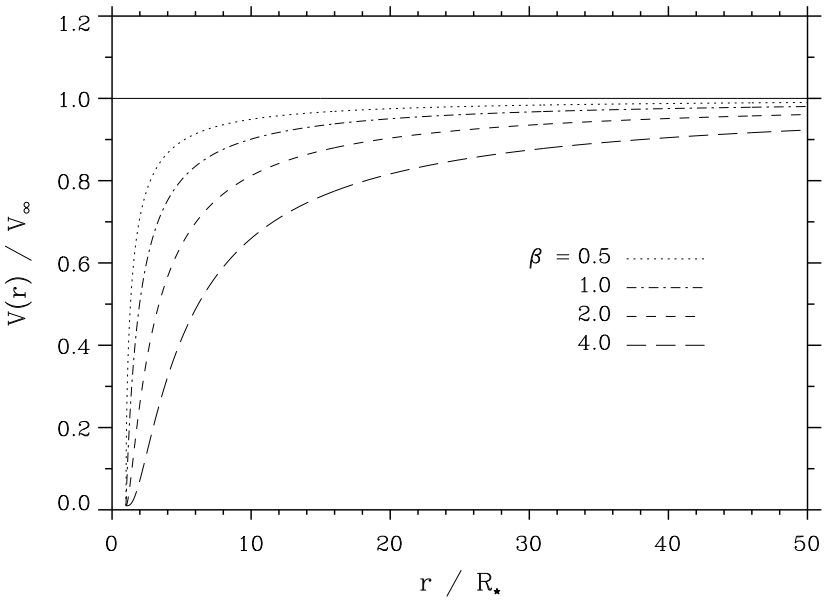

Fig. 5. The beta velocity law given by (15) as a function of radius for $v_0 = 0.01\, v_\infty$ and several values of β.

from the other factors (e.g., $q_{jk}(r)$, $\mathcal{T}_{jk}$) that affect their shapes. Thus, the main parameters associated with the velocity field of the wind, v_∞ and β, can both be determined from the P Cygni profiles of strong UV resonance lines.

Suppose that we have used our favourite computer program to achieve an acceptable fit of the P Cygni profile of an unsaturated UV resonance line. In order to do this, we have had to overcome the usual sort of practical problems, like rectifying the observed data (which can be difficult in the UV due to heavy line blanketing) and allowing for the underlying photospheric line (either by using an observed, purely photospheric template spectrum or by computing the profile in some way). At the end of this process, we've determined:

- the parameters v_0, v_∞, and β that define the velocity law.
- the total optical depth of the resonance transition, $\mathcal{T}_{jk}$, and hence its column depth, $\mathcal{N}_{jk}$, via (14).
- the parameters $\boldsymbol{\alpha}$ describing the distribution of optical depth as a function of velocity (or radius).

How close does this information get us to $\dot{M}$? The column depth can also be determined by direct integration of (11), which, after some rearranging

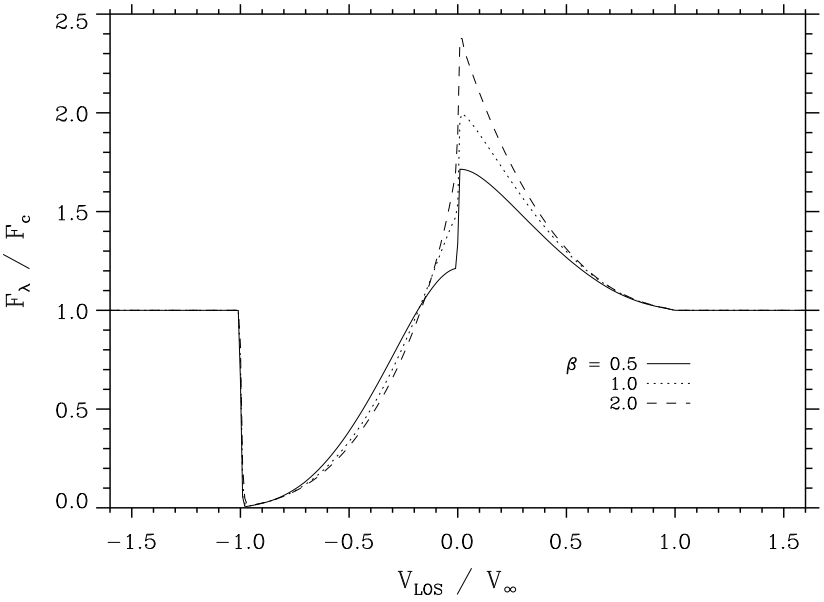

Fig. 6. P Cygni profiles of a strong resonance singlet line calculated for several values of the velocity-law parameter β. More emission results from "slower" velocity laws.

becomes

$$\dot{M} \int_{R_\star}^{\infty} \frac{q_{jk}(r)}{r^2\, v(r)}\, \mathrm{d}r \;=\; 4\,\pi\, \frac{m_k}{X_k} \int_{R_\star}^{\infty} n_{jk}(r)\, \mathrm{d}r \;=\; 4\,\pi\, \frac{m_k}{X_k}\, \mathcal{N}_{jk} \quad . \tag{16}$$

Following Howarth & Prinja (1989), the mean value of $q_{jk}(r)$ can in addition be defined by

$$\overline{q}_{jk} \equiv \frac{\int_{R_\star}^{\infty} q_{jk}(r) / \left[r^2\, v(r)\right]\, \mathrm{d}r}{\int_{R_\star}^{\infty} 1 / \left[r^2\, v(r)\right]\, \mathrm{d}r} = \frac{\int_{R_\star}^{\infty} q_{jk}(r) / \left[r^2\, v(r)\right]\, \mathrm{d}r}{\mathcal{I}(v_0,\, v_\infty,\, \beta)} \quad , \tag{17}$$

and so

$$\dot{M}\, \overline{q}_{jk} \;=\; 4\,\pi\, \frac{m_k}{X_k}\, \frac{\mathcal{N}_{jk}}{\mathcal{I}(v_0,\, v_\infty,\, \beta)} \quad . \tag{18}$$

Everything on the right-hand side has been measured or is otherwise known, with the possible exception of X_k, which has to be determined from photospheric analysis of the star or simply assumed.

However, we ultimately fail to determine $\dot{M}$ because we don't know $\overline{q}_{jk}$: it is simply not possible to measure the ionization fraction of an element on the basis of a single line. Usually, the ionization balance can be constrained by examining the strength of lines from the adjacent stages. Unfortunately,

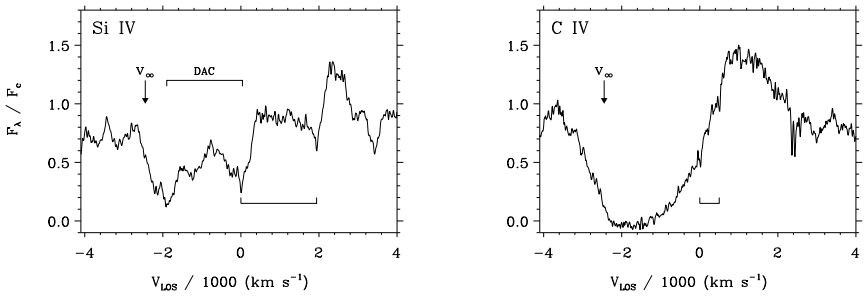

Fig. 7. An IUE spectrum of ξ Per (SWP 34559) showing the P Cygni profiles of two UV resonance lines. Left: the unsaturated Si IV doublet, with a soft blue edge and DACs in the absorption trough. Right: the saturated C IV doublet, with a soft blue edge and an extended black trough. The rest positions of the blue and red components of the doublets are marked; the velocity scale refers to the blue component.

the resonance lines of stages adjacent to those responsible for the observed P Cygni profiles usually fall in the extreme UV region of the spectrum, where the flux of early-type stars is small owing to absorption in the Lyman continuum of interstellar hydrogen. To make matters worse, theoretical predictions are not especially helpful: if the prediction is that the ion is the dominant stage, then the P Cygni profile is invariably saturated, and only provides a lower limit on $\mathcal{N}_{jk}$. Alternately, if the ion is a trace stage, theoretically predicted values of its q_{jk} are uncertain since they depend sensitively on the details of the calculation (e.g., inclusion of X-rays from shocks, inclusion of line blanketing in the extreme UV region of the spectrum; see Pauldrach et al. 1994) that are not yet considered to be completely reliable (Groenewegen & Lamers 1991). The only option at present is to try to estimate $\overline{q}_{jk}$ by comparing the values of $\dot{M}\overline{q}_{jk}$ obtained from UV resonance lines with mass-loss rates determined from other diagnostics that are not sensitive to ionization (e.g., radio continuum measurements; see Howarth & Prinja 1989). So, for the moment, we are left in the unsatisfying situation that the best qualitative tracers of the diffuse gas in stellar winds are not the best estimators of the mass-loss rate.

To compound these difficulties, there are also complications with the determination of the velocity law from the P Cygni profiles of UV resonance lines. The problem is that the blue edges of the absorption trough of strong lines are rarely observed to be as steep and well defined as illustrated in Figs. 4 and 5, but approach the continuum more gradually. Consequently, the interpretation of the position of the blue edge as a "clear-cut" diagnostic of v_∞ is compromised. This deviation from the classical P Cygni shape is illustrated in Fig. 7 for the Si IV and C IV resonance doublets of the O7.5

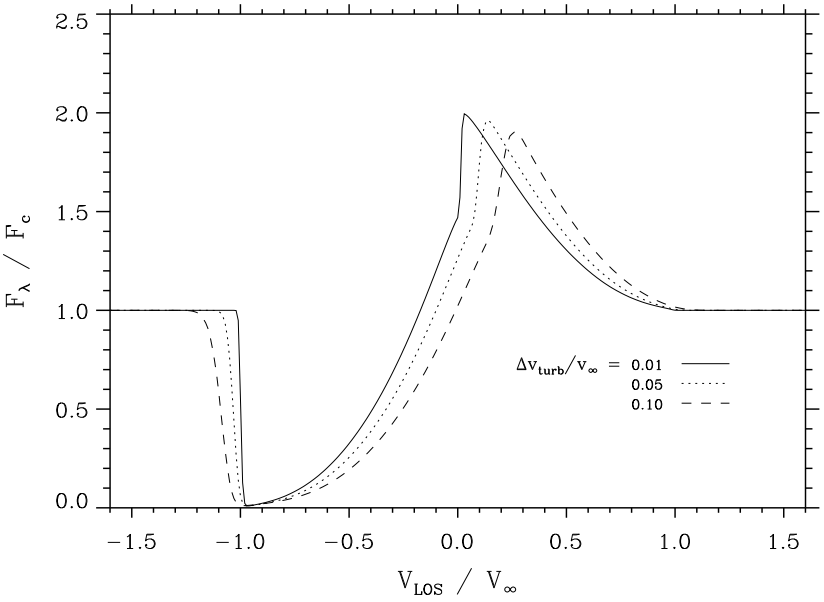

Fig. 8. P Cygni profiles of a strong resonance singlet line calculated for several values of the velocity dispersion parameter $\Delta v_{\rm turb}$. These calculations assume that the dispersion is constant throughout the wind, and show that increasing the size of $\Delta v_{\rm turb}$ softens the blue edge, extends the region of saturation in the absorption trough, and shifts the emission peak redward.

giant ξ Persei; see also the C IV profile of 9 Sge in the top panel of Fig. 1.

The "softening" of the blue edge of the absorption trough is generally interpreted as an indicator that another, more chaotic velocity field is superimposed upon the mean expansion of the wind (§3.6). This extra velocity field is usually referred to as "turbulence", though it is preferable to think of it as a velocity dispersion that acts as an extra broadening agent for the material in the wind rather than turbulence in a strict hydrodynamical sense. Purely for convenience, it is assumed to have a Gaussian distribution that is characterized by its root-mean-square dispersion parameter, $\Delta v_{\rm turb}$, which can be added in quadrature to the $v_{\rm th}$ to produce a net broadening that does not require substantial changes to the SEI approach to calculating line profiles. The dispersion parameter $\Delta v_{\rm turb}$ may be taken to be constant throughout the wind (as in Groenewegen & Lamers 1989) or as an increasing function of radius (as in Haser 1995 or Haser et al. 1995; this tends to suppress the redshift of the emission lobe, which is overestimated for some of the fits presented by Groenewegen & Lamers 1989). Fig. 8 illustrates the effect of a constant broadening on the P Cygni profile of a strong singlet, and shows in particular the "softening" of the blue edge of the absorption trough by the extra

broadening, which shifts the maximum blue-shifted velocity in the absorption trough to $v_\infty + n\,\Delta v_{\rm turb}$ (where $n \lesssim 3$ depends on the total optical depth of the line). Thus, in practice, v_∞ is *overestimated* if it is assumed to correspond to the blue edge of the trough. Since the determination of β depends on the shape of the emission lobe, it will also be affected by the inclusion of turbulent broadening. In practice, this complication just means that $\Delta v_{\rm turb}$ must also be determined simultaneously with v_∞ and β by a detailed fit to the observed profile.

However, Fig. 7 also shows that there are several additional peculiarities associated with the UV P Cygni profiles of ξ Per. First, the absorption trough of the strong C IV doublet exhibits an extended interval of blackness (a "black trough"), something that we previously noted is impossible for a smooth wind. Second, the absorption trough of the unsaturated Si IV line is disrupted by the presence of narrow optical depth enhancements, which are called "discrete absorption components" (DACs). These three peculiarities – a soft blue edge, black troughs, and DACs – occur very commonly among OB stars; as discussed in §3.6, they are all evidence for the presence of time-dependent structure in the stellar wind of most or all early-type stars. As such, they tend to undermine the picture of the stellar wind as a smooth, spherically symmetric, steady outflow that currently serves as the basis for quantitative modelling.

3.5 Optical Emission Lines

The main diagnostics of hot-star winds at optical wavelengths are the broad emission features that are found in transitions of H, He I, and He II. Hα is typically the strongest of these features, though lines like He I λ5876 and He II λ4686 are also important, particularly in spectra of O-type supergiants. A wide range of morphologies can be observed in these profiles (see Fig. 1), including partially filled photospheric absorption lines in the case of weak winds. The information about the structure of the stellar wind contained in them is comparable to the information contained in UV resonance lines: for a spherically symmetric wind, the overall strength of the emission indicates the amount of material, while the shape of the line profile depends on how the material is distributed.

However, there are also significant differences compared to resonance lines. From a practical point of view, the ρ^2 dependence of recombination lines means that they are not sensitive diagnostics of rarefied gas. Consequently, they are not well suited to determining v_∞, and in practice this parameter must be obtained from UV resonance lines. At the same time, their comparative weakness is partially offset by the relative ease with which high resolution, high signal-to-noise ratio (S/N) spectroscopic observations can be obtained from ground-based observatories. Since the shape of the line profile can be defined quite precisely from such high-quality data, very weak, high velocity emission wings can be used to determine $\dot{M}$, providing that emission

above the continuum is present. Similarly, the height and width of the central part of the line profile can be used to constrain the β-exponent of the velocity law, since slower velocity laws produce stronger and narrower central emission peaks. Although ground-based observations of Hα (and He I λ5876) are frequently contaminated by blending with dense concentrations of telluric lines (mostly due to water vapour) and sometimes by nebular emission, effective techniques exist to remove these features from the observed spectrum or otherwise limit their impact on the quantitative analysis of the spectra.

Unfortunately, the optical emission lines are a much more complicated case to analyze quantitatively. On the positive side, we know from the outset that H and He are completely ionized until spectral types near A (for H) or early B (for He), so that the main stumbling block encountered for resonance lines is entirely avoided for optical emission features. However, on the negative side (and in contrast to the resonance lines), the excitation balance governing the transition of interest is not known a priori, and detailed non-LTE calculations of the statistical equilibrium in the accelerating atmosphere are required to determine the relevant level populations. The non-LTE population of level i in ion j of element k, n_{ijk}, is often expressed in terms of its LTE value, n^*_{ijk}, and its "departure coefficient", $b_{ijk} \equiv n_{ijk}/n^*_{ijk}$, so that

$$n_{ijk} \;=\; b_{ijk}\, n^*_{ijk} \;=\; b_{ijk}\, n_{0(j+1)k}\, n_e\, \Phi_{ijk}\,(T_e) \quad , \tag{19}$$

where $n_{0(j+1)k}$ and n_e are the number densities of the ground state of the next higher ionization stage and electrons, respectively, and $\Phi_{ijk}(T_e)$ is the Saha-Boltzmann factor defined by Mihalas (1978; equation 5–14), which depends on the electron temperature (T_e) and the difference in energy between state i and the continuum of ion j. Analogous expressions for the populations of the lower and upper levels of a line transition can be substituted into (10) to obtain the Sobolev optical depth in the supersonic part of the wind. For the important case of Hα, $(l, u) = (2, 3)$ and we obtain

$$\begin{aligned}
\tau_{23}\,(r) &= \left(\frac{\pi\, e^2}{m_e\, c}\right)\, f_{23}\, g_2\, \lambda_{23}\, \left(\frac{n_2}{g_2} - \frac{n_3}{g_3}\right)\, \left(\frac{\mathrm{d}v}{\mathrm{d}r}\right)^{-1} \\
&\propto n_{\rm H}\, n_e\, \left[b_2\, \Phi_2\,(T_e) - b_3\, \Phi_3\,(T_e)\right]\, \left(\frac{\mathrm{d}v}{\mathrm{d}r}\right)^{-1} \\
&\propto \left(\frac{\rho}{m_{\rm H}}\right)^2 \left(\frac{4X^2 + I_{\rm He} XY}{4}\right) \left[b_2\, \Phi_2\,(T_e) - b_3\, \Phi_3\,(T_e)\right] \left(\frac{\mathrm{d}v}{\mathrm{d}r}\right)^{-1}
\end{aligned} \tag{20}$$

where the subscripts $j = 0$ and $k = 1$ have been suppressed; we have noted that n_{011} is the number density of protons in the wind, which in turn is given by the number density of hydrogen, $n_{\rm H}$; and we have made the approximation $n_e \approx n_{\rm H} + I_{\rm He}\, n_{\rm He} = (\rho/m_{\rm H})\,(X + I_{\rm He} Y/4)$, where $(X,\, Y) \equiv (X_1,\, X_2)$ are the abundances of hydrogen and helium by mass fraction, and $I_{\rm He}$ is the number of electrons released per helium ion ($I_{\rm He} = 2$ for O and early B-type stars). Equation (20) emphasizes the ρ^2 dependence of the optical depth in Hα, and

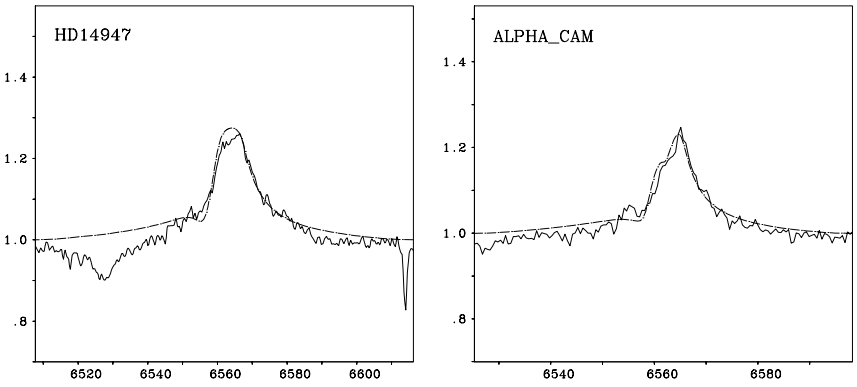

Fig. 9. Fits to observed Hα profiles by Puls et al. (1996). Left: HD 14947 (O5 If$^+$; $\dot{M} = 7.5 \times 10^{-6}\,\mathrm{M}_\odot\ \mathrm{yr}^{-1}$; $\beta = 1.0$). Right: α Cam (O9.5 Ia; $\dot{M} = 5.2 \times 10^{-6}\,\mathrm{M}_\odot\ \mathrm{yr}^{-1}$; $\beta = 1.1$).

shows the explicit dependence of recombination processes on T_e through the Saha-Boltzmann functions.

The observed profile of an optical emission line typically includes significant contributions from the quasi-static photospheric layers, the zone that spans the sonic point of the wind, and the supersonic region of the wind, and the necessity of calculating non-LTE departure coefficients over such a large line-forming region represents an imposing computational challenge. In particular, the Sobolev approximation is not applicable in the deepest of these layers, where the velocity gradient of the expansion is small; and the artifice of dividing the line formation regions into a hydrostatic photosphere and a supersonically expanding wind (the "core-halo" approach) does not treat the density and velocity structure of the transition zone properly. Moreover, radiative couplings with other bound-bound transitions (e.g., the blending of He II λ6560 with Hα) or the complex effects of line blocking in the far UV (in the case of He II λ4686) must also be incorporated. Puls et al. (1996) provide a comprehensive discussion of all these problems, with special emphasis on the formation of Hα profiles in the winds of early-type stars.

These complications can be treated rigorously only in the framework of "unified model atmospheres", which perform complete non-LTE treatments of moving atmospheres without introducing artificial distinctions between the photosphere and the wind (Gabler et al. 1989). Although the initial calculations of such models were quite cumbersome, more efficient algorithms (that still use a variety of approximations) have been developed in the past

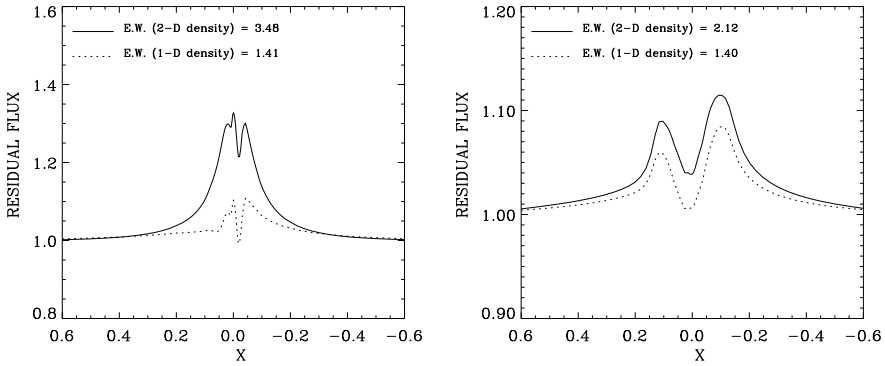

Fig. 10. Hα profile strength and morphology as a function of inclination angle for 1D (dotted) and 2D (solid) density distributions, a fixed $\dot{M} = 6 \times 10^{-6}$ $M_\odot$ yr^{-1}, and $v_{\rm rot}$=250 km s^{-1}. Left: $i = 0°$. Right: $i = 90°$. The abscissa is $V_{\rm LOS}/v_\infty$ in the reference frame centered on the star (opposite to previous figures); note the difference in ordinate scales. In both cases, the 2D distributions produce more emission from the same amount of wind material; the difference is particularly dramatic for the "pole-on" orientation. See Petrenz & Puls (1996) for details.

few years, and several programs are now capable of performing interactive (or nearly interactive) modelling of optical emission lines: see, e.g., de Koter et al. (1993), Schaerer & Schmutz (1994), and Santolaya-Rey et al. (1997). Alternately, Puls et al. (1996) describe a very efficient hybrid approach that can be used to model line profiles of a particular wind feature for objects that span a limited range of spectral types by using parameterized fits to the radial distribution of the relevant departure coefficients, which are obtained from a grid of unified model atmospheres. Puls et al. (1996) applied this approach to the determination of $\dot{M}$ from Hα profiles of a large sample of O stars, for which the other fundamental stellar parameters ($T_{\rm eff}$, $\log g$, $R_\star$, Y, $v \sin i$, and v_∞) had previously been determined by the methods of "quantitative spectroscopy". Fig. 9 shows that very good fits to observed spectra can be obtained, which result in precise determinations of $\dot{M}$ and β.

However, the *accuracy* of these determinations depends rather strongly on the correctness of the assumptions of spherical symmetry and homogeneity, i.e., on whether the assumed distribution of material in the wind is a good approximation for the real distribution. Consider, e.g., two equal volumes of a uniform, spherically symmetric wind that are located at the same radial distance from the star. Let the density in one volume be half the density in a corresponding volume of a uniform wind (i.e., $\Delta m_1 = 0.5\,\rho_0\,\Delta V$, where ρ_0 is the density of the smooth wind) and the density in the other be 50% more ($\Delta m_2 = 1.5\,\rho_0\,\Delta V$). The total mass in these two "clumps" is the same as in the corresponding volumes of the smooth wind, but since the number of recombinations scales with ρ^2, the emission that arises from them is propor-

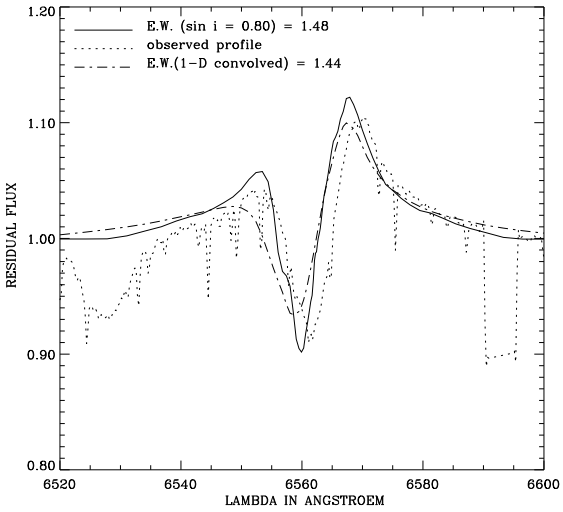

Fig. 11. Fits of 1D (dot-dash) and 2D (solid) density distributions to the Hα profile of the O4 supergiant ζ Puppis (dotted). Figure courtesy of P. Petrenz.

tional to $(0.5^2 + 1.5^2)\,\rho_0^2 = 2.5\rho_0^2$, which is 1.25 times that from the smooth wind. If we attempted to model the emission from the "clumped" volumes by assuming a smooth density distribution, we would mistakenly attribute this "excess" emission to a higher density. In this case, we would overestimate the amount of material they contain by $\sim$12%.

Similarly, the mass-loss rates of winds that are structured or aspherical will be *systematically overestimated* if their optical emission lines are interpreted in terms of a density distribution that is smooth and spherically symmetric. Both these complications are expected to occur in the winds of early-type stars: clumping because the line-driving mechanism is unstable (see, e.g., Owocki 1990), and asphericity because sufficiently rapid rotation concentrates the material of the wind towards a preferred plane (e.g., the equatorial plane in the "wind-compressed disk" [WCD] or "wind-compressed zone" [WCZ] model discussed by Bjorkman in his lectures in this volume). Fig. 10 compares the Hα line profiles computed from a smooth, 1D density distribution with those from the 2D density distribution appropriate to a WCZ. The total amount of material in the wind is the same in both cases, but is concentrated towards the equatorial plane in the WCZ models, with the result that more emission is produced by the 2D models. The two panels of Fig. 10 also show that there is a further dependence on the angle at which the WCZ is viewed, with much stronger emission occuring when the star is seen "pole on" ($i = 0°$) because the area the equatorial concentration presents to the observer is maximized in this configuration.

Petrenz & Puls (1996) have considered the impact that aspherical density

distributions have on the determination of stellar wind parameters by fitting synthetic profiles computed from 1D (spherically symmetric) wind models and 2D (WCZ) models to observed Hα profiles. Fig. 11 shows that both models provide fits of comparable quality to the Hα profile of O4 supergiant ζ Puppis, which is a rapid rotator ($v \sin i = 210$ km s^{-1}) for its luminosity class. However, the wind parameters inferred from the fits are substantially different: the 1D model gives ($\dot{M}$, β) = (5.9×10^{-6} M$_\odot$ yr^{-1}, 1.15), while the 2D model gives ($\dot{M}$, β) = (3.4×10^{-6} M$_\odot$ yr^{-1}, 2.00) and an inclination of 53 degrees. Thus, in this case, the assumption of spherical symmetry implies that $\dot{M}$ is overestimated by $\sim$70%, and that the velocity law is faster than the values obtained from 2D models. Since early-type stars tend to be rapid rotators, WCZs are expected to occur commonly (Bjorkman & Cassinelli 1993; Ignace et al. 1996): failure to account for them (or other structures) when modelling recombination lines will result in mass-loss determinations that are systematically overestimated.

3.6 Time-Dependent Structure in Hot-Star Winds

In §3.4, we noted three common peculiarities in the absorption troughs of the P Cygni profiles of the UV resonance lines: soft blue edges, extended regions of blackness, and DACs. Although these deviations from the expected morphology are present in some of the earliest observations from the Copernicus satellite observatory (e.g., Morton 1976), they did not initially attract much attention. Lamers et al. (1982) noticed that DACs occurred quite commonly in "snapshot" observations of a sample of OB stars obtained with Copernicus, a result that was soon confirmed with the International Ultraviolet Explorer (IUE) satellite observatory (Prinja & Howarth 1986). However, it was not until IUE began to provide routine monitoring capability that the DACs were recognized to be fundamentally a time-dependent phenomenon. Subsequent work has shown that the shape and strength of the blue edge of the absorption trough are also variable.

The characteristic behaviour of DACs is illustrated in Fig. 12, which shows a series of 24 spectra of the Si IV resonance doublet of ξ Per obtained with IUE by H. F. Henrichs and collaborators over $\sim$2.6 days in 1988 October. The spectra are presented in the form of a grey-scale image where darker shades represent less flux (excess absorption) and lighter shades represent more flux with respect to the mean spectrum, which is plotted below the image. This format, which is often called a "dynamic spectrum" (a term borrowed from radio astronomers who monitor pulsars), is an ideal way to show the progressive evolution of weak features through a large number of spectra. A given DAC first becomes visible in both components of the doublet as a broad optical depth enhancement at an intermediate velocity, but is not accompanied by significant variations in the emission lobe. It accelerates blueward through the trough and becomes narrower as it reaches its asymptotic velocity, which is approximately equal to v_∞. The time scale for the acceleration is $\sim$1 day

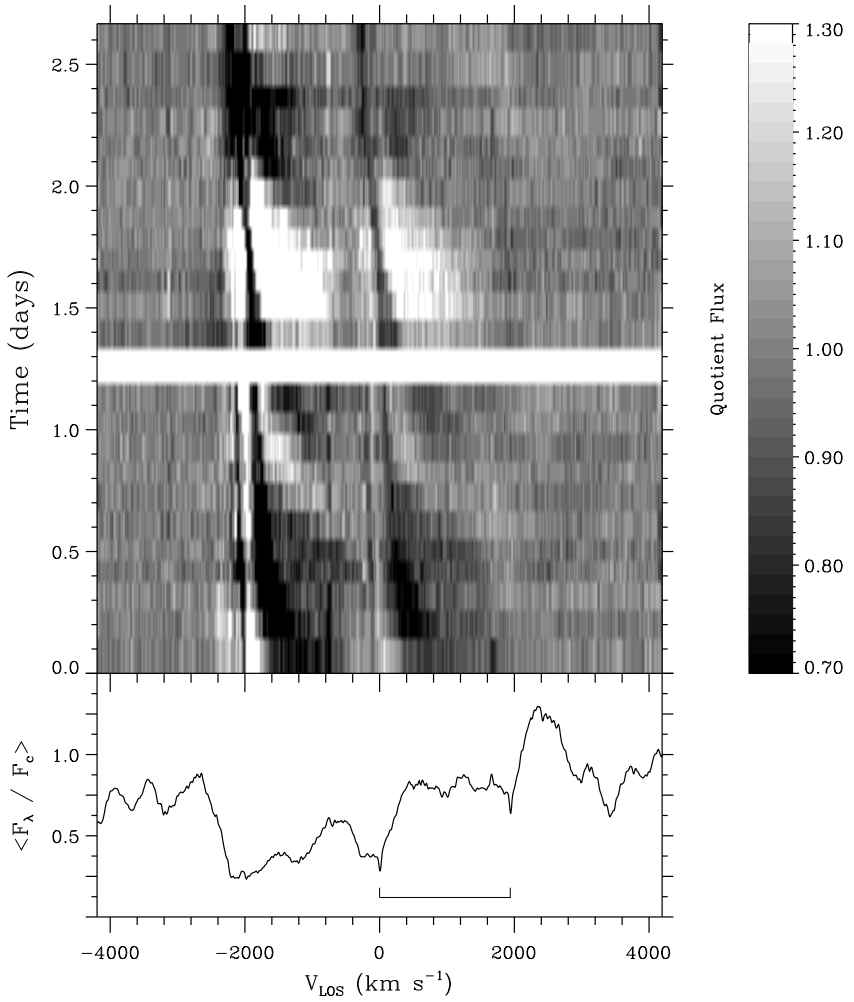

Fig. 12. Dynamic spectrum of the Si IV resonance doublet of ξ Per showing the blueward acceleration of two DACs. Individual spectra in the time series have been divided by the mean in order to enhance the contrast of the variations. The rest positions of the components of the doublet are indicated; the behaviour of the DACs is the same in both components. The white strip near the middle of the time series denotes a significant gap in the time sampling.

in the case of ξ Per, which is quite slow compared with the characteristic flow time of its wind: $t_{\rm flow} \gtrsim R_\star/v_\infty \approx 1$ hour. For ξ Per, the recurrence time between the appearance of strong DACs is ~ 2 days; in the time series illustrated in Fig. 12, a weaker component may be present in between the stronger ones.

Although ξ Per is one of the most intensively studied objects (Prinja et al. 1987; Henrichs et al. 1994), its behaviour is certainly not unique. Howarth & Prinja (1989) reported the detection of DACs in 80% of the objects in their thorough study of the IUE "snapshot" spectra of 203 O stars; detailed monitoring of a subset of these objects has subsequently shown behavioural patterns that are qualitatively similar to the DACs of ξ Per (Kaper et al. 1996). DACs have also been tracked in the UV spectra of B-type supergiants (e.g., Massa et al. 1995b), a WR star (Prinja & Smith 1992), and optical P Cygni profiles of O supergiants (e.g., Fullerton et al. 1992; Prinja & Fullerton 1994) and B hypergiants (Rivinius et al. 1997).

The widespread occurrence of DACs implies that at least one of the assumptions of the "standard model" of hot-star winds – stationarity – is not valid. From (11) and (12), we see that a DAC could be produced at a particular position in the absorption trough by enhancing $\tau_{\rm UV}$ in one of three ways:

- locally *increasing* the ionization fraction, $q_{jk}(r)$.
- locally *increasing* the density, $\rho(r)$, either as a spherically symmetric shell or as a "clump" of arbitrary shape.
- *decreasing* the velocity gradient ($\mathrm{d}v/\mathrm{d}r$) over some range of radii, thereby producing a "plateau" in the radial velocity law.

When DACs can be observed in unsaturated lines with very different ionization energies (e.g., Si IV and N V), they usually occur at the same velocity and evolve in the same way; consequently, changes in the ionization fraction are generally not thought to be responsible for the absorption excess (but see Prinja et al. 1997 for an important exception). Since variations in the emission lobe are rarely observed, dense shells are more or less ruled out, though big clumps that cover most of the stellar disk do seem to be required to explain the depth of some DACs (and possibly also the [presumably related] phenomenon of "moving bumps" in the emission lines of WR stars; see Moffat et al. 1988). In any case, each of these methods of producing a DAC implies that there is some extra "structure" in the wind, and consequently the validity of the remaining assumptions of the "standard model" (homogeneity and spherical symmetry) are also dubious. A crucial issue is to assess the impact that these time-dependent wind structures have on the determination of mass-loss rates, which first requires that the origin and nature of the wind structures be clarified.

Much of this structure is believed to be the result of a potent instability that is intrinsic to the line-driving mechanism; i.e., the winds of early-type stars are variable by virtue of the way they accelerated. The origin

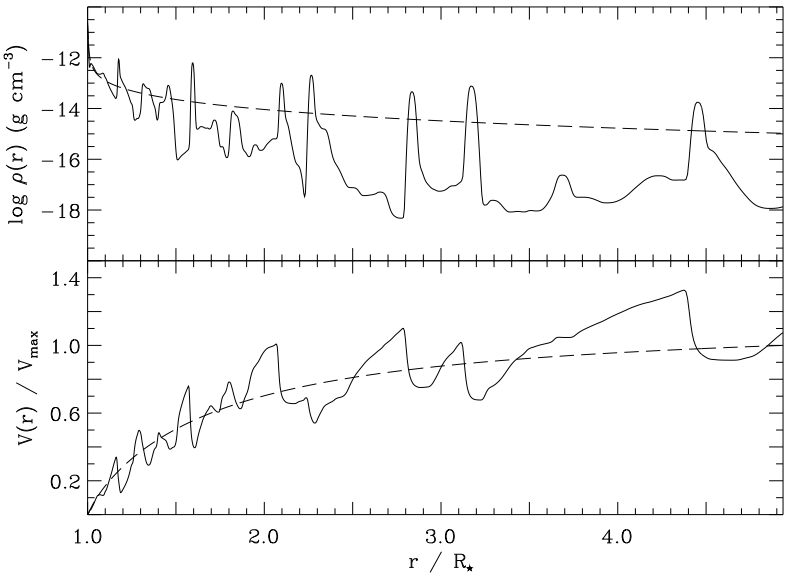

Fig. 13. The density and velocity distributions obtained from time-dependent simulations of a hot-star wind that is disrupted by the line-driven instability. The dashed line indicates the distribution of density and velocity from a comparable stationary model. From Puls et al. (1993).

of this instability is described in very clear, graphical fashion by Owocki (1992). Although this instability has been recognized for a long time (e.g., Lucy & Solomon 1970; MacGregor et al. 1979; Carlberg 1980; Owocki & Rybicki 1984), it has only recently become possible to study its impact on the structure of a stellar wind by following its nonlinear growth in radiation hydrodynamics simulations (Owocki et al. 1988, Feldmeier 1995). These computations are technically very challenging, because the line-driven instability grows most strongly on small spatial scales, and consequently the Sobolev approximation cannot be used to simplify the radiative transfer. The current generation of simulations are limited to one spatial dimension, which means that the structures that result from them consist of spherically symmetric shells.

Fig. 13 shows a typical "snapshot" of $v(r)$ and $\rho(r)$ in a model of a hot-star wind at a time approximately 15 hours after basal perturbations in the form of a coherent photospheric sound wave were introduced. The deep-seated perturbations are amplified by the instability, which results in small amounts of gas being driven to very high velocities. This high-velocity, rarefied gas ultimately crashes into the more slowly moving material in front of it (i.e.,

at larger radii), and the resulting compression concentrates the wind into a series of dense clumps (i.e., shells in these 1D simulations). Thus, instead of the smooth, monotonic distributions expected from the stationary model, the material of the wind is inhomogeneously redistributed into a series of dense shells that are separated by regions where there is very little gas. The velocity of the rarefied gas can exceed v_∞, while the dense shells move at about the speed of the gas at the same radii in an unstructured wind.

The nonmonotonic density and velocity distributions in Fig. 13 introduce some interesting complications to the picture of line formation that was outlined in §3.2 and 3.3. Since the velocity law is no longer a smoothly increasing function of radius, a photon will not necessarily be free to travel unimpeded through the wind after it works its way through the first scattering zone (as was the case, e.g., in the discussion of Fig. 4). Instead, it might encounter other clumps of material, possibly at very different positions in the wind but nonetheless moving with velocities "tuned" to the resonance line transition, which therefore permits further scattering interactions to occur. The possibility for multiple interactions can be easily seen from Fig. 13, since a horizontal line at a fixed velocity (which represents a fixed photon frequency in the observer's frame) intersects the computed velocity distribution at several widely separated radii: e.g., a line at $v(r)/v_{\rm max}$ (where $v_{\rm max} \equiv v_\infty$) of 0.8 intersects the velocity law at values of $r/R_\star$ near 2, 2.5, 3.0, and 3.4, instead of the single value ($\sim$2.3) in the case of a smooth, monotonically expanding wind.

As Lucy (1982) first realized, the net effect of these multiple interactions is to increase the amount of back-scattering. Consider again a horizontal line drawn across the velocity distribution in Fig. 13, and suppose for simplicity that scatterings only occur in the radial direction (i.e., $\cos\psi = \pm 1$ in the notation of Fig. 4). Further suppose that at each scattering surface there is roughly a 50% chance that a photon will be forward-scattered and a 50% chance that it will be back-scattered. Consequently, after n such scatterings, the fraction of the original beam of continuum photons that is still travelling in the forward direction is $(0.5)^n$, while the remainder have been back-scattered towards the star. In fact, the situation is a bit more complicated, because photons that are back-scattered at scattering surface i can be back-scattered another time when they encounter scattering surface $i-1$ on their inward journey, and so rejoin the outward propagating beam. Nevertheless, the basic point is that essentially all the outward propagating photons will end up being back-scattered towards the star if there are a sufficiently large number of interaction surfaces.

The effects of these multiple and nonlocal interactions can be incorporated into the Sobolev formalism is a straightforward way; see, e.g., Rybicki & Hummer (1978) and Puls et al. (1993). Fig. 14 illustrates the changes in the structure of the absorption and emission components of the P Cygni profiles of resonance singlets that result from the nonmonotonic (but spherically sym-

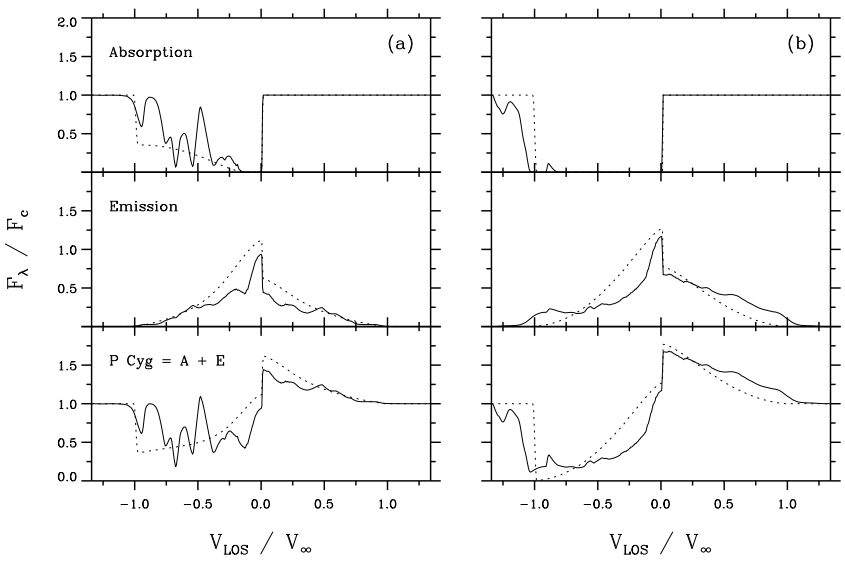

Fig. 14. P Cygni profiles of UV resonance singlets from the structured stellar wind model illustrated in Fig. 13, computed for the case of (a) a moderately strong line and (b) a strong line. The dashed lines indicate the various components of the profiles for the case of the smooth wind illustrated in Fig. 3. DACs are visible in the absorption trough of (a); the soft blue edge extending beyond v_∞ is clearly seen in (b). Changes in the shape of the blue- and red-shifted emission due to increased back-scattering from the multiple interactions in the nonmonotonic velocity law are also evident.

metric) distributions shown in Fig. 13. The clumpy distribution of material is directly visible in the absorption component of an unsaturated line, which shows both excesses and deficits of optical depth (with respect to the absorption trough of a comparable smooth wind) that are due to the dense clumps and the rarefied regions, respectively. Since all the photons are removed from the absorption trough of an intrinsically strong line, these clumpy structures are not visible in its absorption component. However, for a strong line, the small amounts of rarefied gas that have been driven to velocities in excess of v_∞ have sufficient optical depth to produce a shallow, extended, and time-dependent blue edge. The forward-scattered emission components of both moderate and strong lines are generally weaker than the components of a comparable smooth wind at low $V_{\rm LOS}$, which is a direct consequence of the tendency for multiple interactions to preferentially back-scatter photons. Of course, an excess of back-scattering in the *receding* hemisphere tends to produce more photons in the redshifted part of the emission component: this

effect is most clearly seen for the strong line, where the detailed distribution of emission depends on the exact location and density contrast of the clumps. The net result is that the unsaturated lines exhibit absorption components in their absorption troughs and weaker emission lobes, while the strong lines exhibit shallow blue edges that extend beyond v_∞, broad absorption troughs, and stronger emission lobes (which are at least partially due to spherically symmetric geometry implied by Fig. 13).

Evidently, the wind structures that arise in a natural way due to the action of the line-driven instability go a long way towards explaining the time-dependent peculiarities seen in P Cygni profiles:

- DACs can be attributed to the slowly moving dense clumps.
- soft blue edges and blue-edge variability of strong lines can be attributed to the presence of variable amounts of rarefied gas at velocities in excess of the time-averaged value of v_∞. Although the Gaussian velocity dispersion parameter $\Delta v_{\rm turb}$ discussed in §3.4 mimics this effect, it does not incorporate the essential physical ingredients (i.e., strongly driven gas, multiple couplings due to the nonmonotonic velocity field) in a meaningful way, and is therefore of limited diagnostic value. Moreover, the redshift of the emission lobe with increasing values of $\Delta v_{\rm turb}$ (Fig. 8) seems to be an artifact of the ad hoc way in which the velocity dispersion is introduced to the calculation of line profiles: no such shifts occur for the profiles in Fig. 14.
- black troughs occur in strong lines when there are enough structures in the forward hemisphere of the wind to produce complete back-scattering over a range of $V_{\rm LOS}$. The profile in Fig. 14(b) does not exhibit a black trough only because the wind model used to compute it (Fig. 13) does not have enough structure near v_∞; see, e.g., Lucy (1983) and Puls et al. (1994).

These successes are emphasized qualitatively in Fig. 15, which shows synthetic dynamic spectra computed for the full run of a radiation hydrodynamics simulation (Owocki et al. 1994). These synthetic time series show weak variability in the emission lobe, which is largely because the structures are assumed to be spherically symmetric; there are also some very narrow, rapidly evolving features that do not correspond to observed variations. Nevertheless, the general characteristics of DACs in unsaturated lines that accelerate over the course of $\sim$1 day (e.g., in the second half of the time series shown in the left-hand panel) and extensive blue-edge variability (e.g., in the first half of the time series in the right-hand panel) have many points of correspondence with the observed variations of ξ Per (Fig. 12).

However, despite these promising developments, the origin and nature of the DACs is still mysterious. Monitoring campaigns (e.g., Prinja 1988; Kaper et al. 1996) of many objects have linked the acceleration and recurrence of DACs to the projected rotational velocity of the underlying star, which suggests that the wind structures responsible for these spectroscopic features

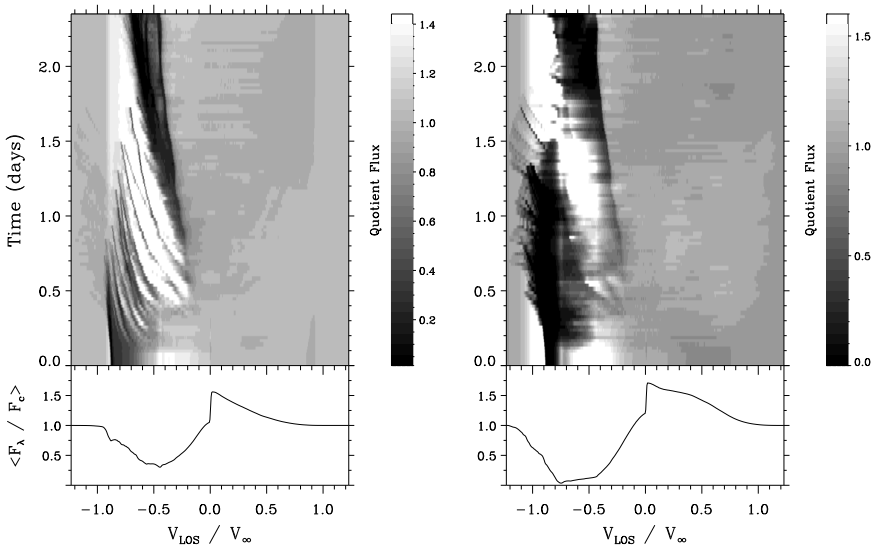

Fig. 15. Dynamic spectra generated from radiation hydrodynamics simulations of the growth of the line-driven instability by Owocki et al. (1994). Left: DAC variability in a line of modest strength. Right: blue-edge variability in a strong line; DAC is also visible since this line is not saturated. Individual spectra in the time series have been divided by the mean in order to enhance the contrast.

might ultimately be controlled by the stellar rotation rate. The recent IUE "MEGA Campaign" (Massa et al. 1995a) tested the strength of this connection directly by monitoring the UV resonance lines of three early-type stars continuously for an unprecedented interval of ∼16 days. In all three cases – most directly for ζ Puppis (Howarth et al. 1995) and the B0.5 supergiant HD 64760 (Prinja et al. 1995) – the time scales for at least some of the wind variability could be tied directly to the estimated rotational period of the star. It is very difficult to understand how structures generated by dynamical processes in the wind (like the line-driven instability) can be tightly coupled to the stellar rotation rate, and the focus of recent work has been on finding alternative ways of generating structures that can rotationally modulate the wind. The corotating interaction regions (CIRs) originally suggested by Mullan (1984) are among the most promising of these alternatives. Hydrodynamical simulations by Cranmer & Owocki (1996) confirm that CIRs can produce DACs that evolve over time scales determined by the stellar rotation rate. Interestingly, they find that the velocity gradient term in $\tau_{\rm UV}$ is responsible for these optical depth enhancements, not the density term. Much more work remains to be done in order to understand the origin of DACs, whether

the mechanism responsible for them can also explain soft blue edges and black troughs independent of the line-driven instability, and what impact these time-dependent structures in the wind have on the determination of mass-loss rates from spectroscopic (and continuum) diagnostics.

4 Continuum Diagnostics

At first glance, continuum measurements may not seem like a very promising method of determining $\dot{M}$, since they contain little information about the velocity law and would thus appear to provide insufficient data to satisfy (1). In fact, flux measurements at single wavelengths in the far infrared and radio region can provide quite reliable estimates of $\dot{M}$, provided that the distance to the star and v_∞ are known. The velocity law can also be determined by measuring the flux distribution at several widely spaced wavelengths. Consequently, the overall usefulness of continuum measurements is limited not so much by the physics of their formation as by the spatial resolution and instrumental sensitivity required to detect intrinsically weak flux levels (typically $\ll 1\,\mathrm{jansky\,[Jy]}$) from distant objects at these wavelengths.

4.1 Free-Free Emission

The contribution of the wind to the flux at infrared and radio wavelengths usually comes from free-free emission (bremsstrahlung) that arises when a free electron moves in the Coulomb field of another charged particle – usually a proton or alpha particle – but does not become bound to it. The electron is accelerated during this interaction, which alters its hyperbolic orbit and results in the absorption or emission of a photon, depending on whether the new orbit has more or less energy than the original. The energy of such interactions is not quantized, and so the photons from many such interactions will be emitted with a continuous spectrum: since the radiation field results from a collisional coupling between particles that define the thermal energy reservoir of the material in the wind, the relevant distributions are driven towards their LTE values. In particular, the source function for the emitted spectrum is the Planck function, $B_\nu(T_e)$, and the free-free emission coefficient is just

$$j_\nu^{\mathrm{ff}} = \alpha_\nu^{\mathrm{ff}}\, B_\nu(T_e) \quad . \tag{21}$$

Derivations of the free-free absorption coefficient, α_ν^{ff}, can be found in standard texts (e.g., Rybicki & Lightman 1979, Chapter 5); in cgs units, it is given by

$$\alpha_\nu^{\mathrm{ff}} = 3.7 \times 10^8\, T^{-1/2}\, Z^2\, n_e\, n_i\, \nu^{-3} \left(1 - e^{-h\nu/kT}\right) g(\nu, T) \quad \left[\mathrm{cm}^{-1}\right] \quad , \tag{22}$$

where Z is the mean charge per ion; n_e and n_i are the number densities of electrons and ions, respectively; $g(\nu, T)$ is the Gaunt factor (i.e., the correction factor needed to bring the free-free absorption cross-sections derived

semi-classically into agreement with their quantum mechanical values); and all other symbols have their conventional meanings. For infrared and radio frequencies, $h\nu \ll kT$, and the correction for stimulated emission simplifies to $(1 - e^{-h\nu/kT}) \approx (h\nu/kT)$, whence

$$\alpha_\nu^{\rm ff} = 1.8 \times 10^{-3}\, T^{-3/2}\, Z^2\, n_e\, n_i\, \nu^{-2}\, g\,(\nu, T) \quad \left[{\rm cm}^{-1}\right] \quad . \tag{23}$$

Consequently, at these frequencies $\mathrm{d}\tau_\nu^{\rm ff} = \alpha_\nu^{\rm ff}\, \mathrm{d}r \propto \nu^{-2}$ if the weak functional dependence of the Gaunt factor on frequency is neglected ($g \propto \ln[T^{1.5}/\nu]$); alternately, $\tau_\lambda^{\rm ff} \propto \lambda^2$.

This strong dependence of optical depth on wavelength provides the key to understanding the power of continuum methods, since – leaving aside the practical issues of detectability, correction for interstellar extinction, absolute calibration, etc. – it implies that for any $\dot{M}$ it is possible to find a wavelength where $\tau_\lambda^{\rm ff} \approx 1$, i.e., where free-free emission in the wind creates an observable excess of flux over that expected from the stellar photosphere alone. Alternately, observations tuned to progressively longer wavelengths reach $\tau_\lambda^{\rm ff} \approx 1$ at successively larger radial distances from the star. The fast, low-density winds typical of O stars become optically thick at radio wavelengths (2–6 cm), which originate at radii of $\sim$100 $R_\star$ or more, at which point $v(r) \approx v_\infty$. Consequently, uncertainties in the shape of the velocity law do not enter directly into the interpretation of the observed flux, which is sensitive only to the amount of material in the wind. By the same argument, though, the winds of O stars are still optically thin to free-free emission at IR wavelengths, and flux measurements in the IR only provide a measure of the total volume emission; i.e., there is no information about the radial stratification of density (Abbott et al. 1984). Slower, denser winds become optically thick in the continuum at IR (e.g., for LBVs) or even optical wavelengths (e.g., WR stars).

The observed IR and radio fluxes of ζ Puppis are compared with the flux levels expected from the stellar photosphere in Fig. 16. The excess emission due to the wind is evident for wavelengths longer than the M-band ($\sim 5\mu$), and amounts to $\sim$2 orders of magnitude or more in the radio region. Notice, however, that even though ζ Pup is the nearest O star ($D \approx 430$ pc) and has a strong stellar wind, the radio fluxes are only a few millijanskies.

4.2 Spectrum of Free-Free Emission from a Stellar Wind

The continuum flux expected from a homogeneous, spherically symmetric, isothermal wind expanding with constant velocity can be obtained by directly integrating (3), the formal solution to the equation of radiative transfer. The analysis is simpler than that required to compute line profiles, since the source function is known from the outset to be the Planck function for a particular electron temperature (which is usually assumed to be constant through the wind) and there is no need to invoke the Sobolev approximation. Wright

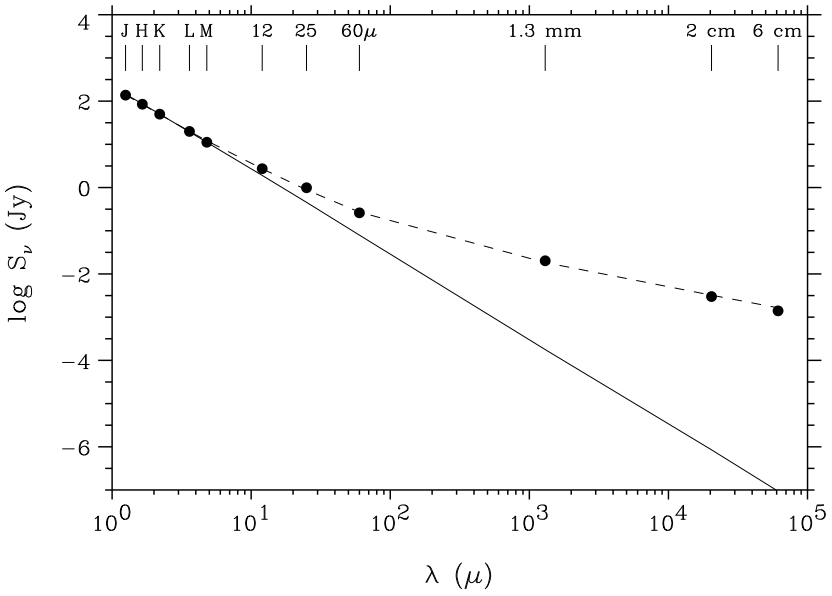

Fig. 16. Observed and predicted continuum flux excesses for ζ Puppis as a function wavelength, with data from Abbott et al. (1984), Lamers et al. (1984), Leitherer & Robert (1991), and Bieging et al. (1989). The solid line indicates the photospheric flux from a unified model atmosphere, while the dashed line is a fit to the flux distribution by (24). Figure courtesy of F. Najarro.

& Barlow (1975) and Panagia & Felli (1975) were the first to perform the integrations (which can be done analytically; see also Abbott et al. 1981 and Lamers & Waters 1984) to obtain the following expression for the flux from free-free emission in the wind:

$$S_\nu = 23.2 \left(\frac{\dot{M} Z}{\mu_i v_\infty} \right)^{4/3} \left(\frac{\gamma g}{D^3} \right)^{2/3} \nu^{2/3} \ \text{[Jy]} \ , \qquad (24)$$

where $\dot{M}$ is in $M_\odot$ yr^{-1}, v_∞ is in km s^{-1}, D is the distance in kpc, and ν is in Hz; and where μ_i, Z, and γ are the mean ionic weight, the root-mean square charge per ion, and the number of electrons per ion, respectively. Lamers & Leitherer (1993) provide a useful table (their Table 4) of values of these parameters for several assumed chemical compositions; for typical Pop. I abundances with complete ionization of H and He, $\mu_i = 1.339$, $Z = 1.149$, and $\gamma = 1.149$.

Equation (24) shows that the flux from free-free emission in a stellar wind $S_\nu \propto \nu^{2/3}$; if the weak frequency dependence of the Gaunt factor is included, the dependence becomes a bit flatter, $S_\nu \propto \nu^{0.6}$. This is intermediate between

the spectral distributions expected for homogeneous plasma that is optically thin ($\propto \nu^{-0.1}$) and thick ($\propto \nu^2$), since both extremes and the complete range of intermediate values contribute to the observed flux at any given frequency. The spectral index is positive since higher frequencies have smaller optical depths ($\tau_\nu^{\rm ff} \propto \nu^{-2}$) and therefore probe systematically deeper layers of the wind, where higher densities produce comparatively more free-free emission.

Equation (24) can be rearranged to obtain a simple expression for the mass-loss rate,

$$\dot{M} = 0.095\,\mu_i\,v_\infty\,\left(Z^2\,\gamma\,\nu\,g\,(\nu,T)\right)^{-1/2}\,D^{3/2}\,S_\nu^{3/4}\quad\left[{\rm M}_\odot\ {\rm yr}^{-1}\right]\ , \qquad (25)$$

which emphasizes that both v_∞ and D must be known by some other means in order to convert S_ν to $\dot{M}$. Otherwise, the expression appears to be quite model independent and straightforward to evaluate. This apparent simplicity is slightly misleading, since the abundances and ionization state of the wind need to be known in order to calculate Z and γ, which implies that the temperature structure must be known. The assumptions of isothermality, Pop. I abundances, and complete ionization are entirely adequate for O-type stars, but may require modifications for objects with denser winds or weaker radiation fields, particularly when recombinations occur for a dominant species, or in the winds of evolved objects with different chemical compositions.

Fig. 16 shows that the spectral distribution predicted by (24) fits the observed excesses at IR and radio wavelengths very well, which in turn confirms that it originates from free-free emission in the wind. In principle, the flux excess at any wavelength where the wind is opaque is sufficient to determine $\dot{M}$ via (25). When measurements at several widely spaced wavelengths are available, the density stratification (or, equivalently, the velocity law) can be probed; see, e.g., Runacres & Blomme (1996). For a distance of 435 pc and v_∞= 2200 km s^{-1}, the fit to the flux distribution of ζ Pup in Fig. 16 gives $\dot{M} = 3.1 \times 10^{-6}\,{\rm M}_\odot\ {\rm yr}^{-1}$, which is in good agreement with the value derived by fitting the 2D density distribution to the Hα profile shown in Fig. 11. The value of β derived from wavelength dependence of the excess is 1.4, somewhat "faster" than the velocity law determined by the fit of the 2D model.

4.3 Mass-Loss Rates from Continuum Observations

Starting with the pioneering work of Barlow & Cohen (1977), much effort has been devoted to using continuum observations of the IR and radio excesses of hot stars to infer mass-loss rates and the radial structure of the stellar wind. Unfortunately, the winds of OB stars are typically optically thin at the near-IR wavelengths accessible from the ground, and consequently the IR excesses are small (see, e.g., Figs. 16 and 17) and subject to uncertainties from corrections for interstellar extinction and the absolute flux calibration. Even when they exist, the excesses at wavelengths where the wind is optically thin are determined by $\dot{M}$, $v(r)$, and the temperature stratification of the

Table 2. Selected radio continuum studies

Reference	λ (cm)	Telescope [a]	Objects	Yield [b]
Abbott et al. (1980)	6.1	VLA	OBA	6/10
Abbott et al. (1981)	6.1	VLA	OB	6/10
Bieging et al. (1982)	6.1	VLA	WR	8/13
Vallée & Moffat (1985)	2.8	ARO, VLA	O, WR	0/19
Abbott et al. (1986)	2.0, 6.1	VLA	WR	14/23
Bieging et al. (1989)	2.0, 6.1, 20	VLA	OBA	18/88
Leitherer & Robert (1991)	0.13	SEST	OB, WR	7/ 7
Altenhoff et al. (1994)	0.12	IRAM	OB, WR	18/45
Leitherer et al. (1995)	3.4, 6.2	ATCA	OB, WR	10/11
Contreras et al. (1996)	0.7, 3.5, 6	VLA	OB, WR	8/ 8

[a] VLA – Very Large Array; ARO – Algonquin Radio Observatory; SEST – Swedish-ESO Submillimeter Telescope; IRAM – Instituto de Radioastronomia Millimetrica, Spain; ATCA – Australia Telescope Compact Array.
[b] N(detected) / N(observed)

wind, $T(r)$, and it is impossible to disentangle the contributions of each of these parameters uniquely; see, e.g., Abbott et al. (1984) for a clear discussion of these problems. The situation is better for objects with larger values of $\dot{M}$ like LBVs or WR stars, since the wind is opaque at infrared wavelengths. It also improves for far-IR wavelengths accessible to satellite observatories like the Infrared Astronomical Satellite (IRAS) mission of the early 1980s or, more recently, the Infrared Space Observatory (ISO).

Since hot-star winds are opaque at radio wavelengths, measurements of the free-free continuum between ∼1 mm and ∼20 cm provide more useful information about $\dot{M}$. Table 2 lists a selection of continuum studies of hot stars at radio wavelengths. These observations are difficult to make, since high angular resolution is required to isolate the flux from the wind (which is usually a point source; but see White & Becker 1982 for an important exception) and since the expected flux levels are small, both because of the intrinsic weakness of the emission and the large distances typical of early-type stars. Indeed, from a practical point of view, sensitivity is the biggest drawback to radio continuum observations. This is suggested by the low "yields" typical of the studies listed in Table 2, except for samples that are strongly biased towards extreme objects. Bieging et al. (1989) have completed the largest survey of OB stars to date, and it is interesting to note that while they detected 15 of the 23 sources (65%) they observed in a distance-limited sample ($D < 2.5$ kpc; $\delta \geq -40\,^{\circ}$), they only detected 3 more sources in their total

sample of 88 targets, with sensitive upper limits on nondetections of $\lesssim 0.5$ mJy. Thus, it is unlikely that significantly more stars will be detected in the northern hemisphere, though the advent of the Australia Telescope Compact Array will help to enlarge the sample by providing access to the early-type stars in the rich star fields of the southern skies; see, e.g., Leitherer et al. (1995).

The continuum flux excesses at radio wavelengths are generally thought to provide the most reliable estimates of $\dot{M}$ for hot, luminous OB stars, because (1) when it is detectable, the observed free-free emission originates at great distances from the star and is unaffected by uncertainties in the shape of the velocity law; and (2) the emission does not depend on the detailed ionization or excitation equilibrium in the wind, which, in the case of O stars, can be assumed to be completely ionized. Thus, the main difficulties associated with UV resonance lines and optical emission lines are circumvented. Unfortunately, the assumption of complete ionization cannot be justified for stars with $T_{\rm eff} \lesssim 17{,}000$ K owing to the recombination of helium, and in practice a detailed model of the temperature structure of the wind must be used to interpret the radio continuum flux for supergiants later than ~B2. Moreover, since free-free emission is a ρ^2 process, values of $\dot{M}$ determined from (25) are also sensitive to clumping; as in the case of optical emission lines, the presence of structures in a density distribution that is assumed to be smooth will cause $\dot{M}$ to be systematically overestimated.

The most forceful argument *against* clumping being an important source of bias is that when determinations of $\dot{M}$ from Hα profile fitting and radio continuum measurements are both available, they agree reasonably well with each other on average (Lamers & Leitherer 1993; Puls et al. 1993). These diagnostics probe very different radial distances in the wind: Hα is formed predominantly in the first few stellar radii, while the "radio photosphere" is at tens or hundreds of stellar radii, depending on the wavelength of observation and the amount of material in the wind. Since Hα and free-free emission are sensitive to clumping in exactly the same way, their approximate equality implies that either the degree of clumping (i.e., volume filling factor, density ratio) must be preserved over a enormous range of radii, despite the expansion of the wind, or significant clumping is not in fact present. The first alternative is thought to be unlikely (though not proven to be impossible), which implies that significant clumping is not present at any radius in the wind.

However, this line of reasoning is not completely convincing, since the behaviour of clumped material will depend on the mechanism responsible for introducing the inhomogeneity in the first place. In the case of ζ Puppis, e.g., we have already seen how structures like WCZs may be able to resolve the long-standing "factor of 2" discrepancy between the values of $\dot{M}$ determined from Hα (where the equatorial concentration of material is important) and the radio measurements (where the density distribution is more nearly symmetric); yet this is one of the stars that defines the "on average" equality

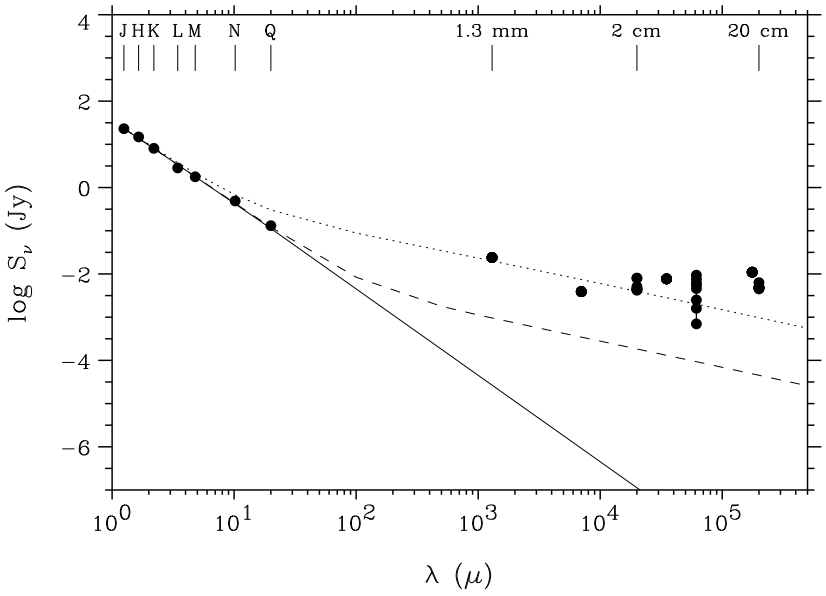

Fig. 17. Observed and predicted continuum flux excesses for Cyg OB2 No. 9 (spectral type O5 If) as a function wavelength, with data from Abbott et al. (1984), Altenhoff et al. (1994), Contreras et al. (1996), Bieging et al. (1989), White & Becker (1983), and Phillips & Titus (1990). The solid line indicates the photospheric flux, while the dashed and dotted lines indicate the predicted flux for mass-loss rates of 4×10^{-6} $M_\odot$ yr^{-1} (which does not fit the radio observations) and 4×10^{-5} $M_\odot$ yr^{-1} (which does not fit the IR observation), respectively. Variability and strong deviations from the flux distribution expected for free-free emission are evident at longer wavelengths. Figure courtesy of F. Najarro.

of $\dot{M}$ determined from these two diagnostics. On a more fundamental level, the widespread variability of hot-star winds strongly suggests that they are inhomogeneous on large spatial scales (§3.6). Until the nature of these inhomogeneities are established more firmly, the impact of wind structures on specific diagnostics of $\dot{M}$ cannot be assessed.

4.4 Nonthermal Radio Emission

An unanticipated difficulty with determining accurate mass-loss rates from radio flux measurements appeared shortly after observations with the Very Large Array began in earnest, when Abbott et al. (1984) recognized that for a minority of targets (initially just 2 stars: 9 Sagitarrii [O4: V((f))] and Cyg OB2 No. 9 [O5 If]) the inferred values of $\dot{M}$ were an order of magnitude larger than the values estimated by other methods. Subsequent multiwave-

length observations showed that the flux distribution for these targets was substantially different from that predicted by (24), with spectral indices $\alpha \leq 0$ (where $S_\nu \propto \nu^\alpha$) rather than the value of +0.6 expected for free-free emission. Both the monochromatic flux levels and the spectral indices were found to be highly variable over intervals of months. These characteristics are illustrated for Cyg OB2 No. 9 in Fig. 17, which shows that – in complete contrast to the case of ζ Pup illustrated in Fig. 16 – the IR and radio flux distributions cannot be fit simultaneously by (24), because there is too much radio emission. Fig. 17 also emphasizes the flatness of the observed radio continuum and the extreme variability, which amounts to more than an order of magnitude at 6 cm.

Abbott et al. (1984) recognized that this behaviour is characteristic of nonthermal radio emission, which contaminates (and in fact dominates) the free-free emission and invalidates the use of (25) to determine $\dot{M}$. Although nonthermal emitters comprise only 24% of the distance-limited sample surveyed by Bieging et al. (1989), they are systematically the most bolometrically luminous stars. They are also systematically stronger radio sources than thermal (free-free) emitters and will therefore tend to be seen to greater distances. Fortunately, they can be distinguished from thermal sources by multiwavelength observations to determine the spectral index α, or by their large variations. Consequently, the complication posed by the existence of nonthermal sources is mostly practical, in that more observing time is required to observe a source at several wavelengths or at several epochs in order to ensure that it is thermal before applying (25) to determine $\dot{M}$.

The origin of the nonthermal emission is unknown, but is probably due to synchrotron emission from electrons that are accelerated to mildly relativistic energies by multiple interactions with strong shocks in the presence of a weak stellar magnetic field (White 1985). The nonthermal source in Cyg OB2 No. 9 has recently been resolved via very-long baseline interferometry (Phillips & Titus 1990), which confirms that the nonthermal component originates at or beyond the radius where the 20 cm free-free continuum is formed and that the emitting volume is large. At the same time, however, Bieging et al. (1989) point out that the nonthermal fluxes at different wavelengths vary in concert, which is difficult to understand in terms of the chaotic, embedded shock model since the "free-free" photospheres at different wavelengths sample very different radii ($\tau_\lambda^{\rm ff} \propto \lambda^2$). On at least one occasion, the nonthermal component of Cyg OB2 No. 9 faded altogether, revealing an underlying spectrum with a spectral index of $\sim$0.6 that permitted Abbott et al. (1984) to derive $\dot{M} = 1.9 \times 10^{-5}$ M$_\odot$ yr^{-1}. Clearly, there is still work to be done to understand the origin of nonthermal radio emission and the implications that its presence has for the structure of hot-star winds.

4.5 The New Frontier: Spectroscopy in the Near and Far IR

The steady improvement in IR detector technology has recently produced an explosion of interest in studying early-type stars spectroscopically in the J, H, and K bands, which have central wavelengths of $\sim$1.25, 1.65, and 2.20μ, respectively. These wavelengths have many advantages for studying hot stars in environments that are highly obscured by dust, like young star clusters (e.g., Hanson et al. 1993) or the Galactic Center (e.g., Najarro et al. 1994). These wavebands contain important lines of H (e.g., the Paschen and Brackett series), He I, and He II, most of which are partially formed in the stellar wind. They generally have a ρ^2 character and resemble optical emission lines, except that they tend to be weaker because they are due to transitions between higher energy levels in their parent atoms. Fig. 18 illustrates the quality of spectroscopic material that can now be obtained at near IR wavelengths by showing the hydrogen lines of Pβ and Bγ (which fall in the J and K bands, respectively) of the LBV HD 160529. Both lines exhibit P Cygni profiles, the detailed shape and strength of which reflect the different emitting volumes appropriate to these transitions.

At still longer wavelengths, IR lines have an important advantage that is not shared by optical emission features, which once again stems from the fact that *continuum* optical depths scale with λ^2. As a result, the "effective photosphere" is a strong function of radius for IR wavelengths beyond the limit where the wind first becomes opaque. Line profiles are only formed at radii that are *larger* than the effective photosphere, and (as we have seen) they can be used to determine the velocity law and density structure starting from that point. Since the (optically thick) continua associated with progressively longer wavelengths form at systematically greater distances from the star, the wind lines at longer wavelengths are formed at larger velocities (i.e., more blue-shifted $V_{\rm LOS}$). Consequently, the information provided by IR wind lines in different wavelength intervals is not redundant, and can be used to piece together the velocity and density structure of the wind – providing that the underlying continuum is optically thick.

Fig. 18 shows that the Pβ and Bγ lines of HD 160529 are not systematically offset from each other: despite its enormous mass-loss rate (1.3×10^{-5} $M_\odot$ yr^{-1}, according to Leitherer et al. 1995), its J and K band continua are not optically thick. Instead, observations at wavelengths in the satellite IR are required to achieve this "infrared advantage", which even then can only be applied to the stars with the densest winds. Despite these caveats, this method promises to become an important new probe of the structure of the outflows from these stars. Indeed, observations of the H and He I lines in the 2.4–45μ region obtained with the short-wavelength spectrometer on board ISO have already provided detailed insights into the wind of the famous LBV P Cygni (Lamers et al. 1996).

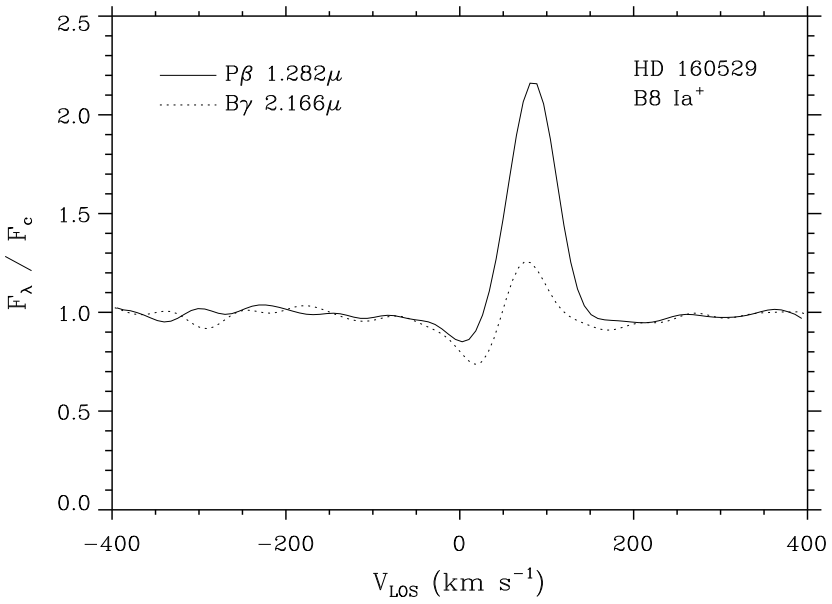

Fig. 18. Infrared P Cygni profiles of Pβ (in the J band) and Bγ (in the K band) for HD 160529. These high-resolution spectra were obtained with the Fourier Transform Spectrometer of the Canada-France-Hawaii Telescope; the small undulations in the continuum are artifacts ("ringing") typical of FTS spectra.

5 Summary and Outlook

It should be clear from the preceding discussion that no single diagnostic provides a completely reliable measurement of the mass-loss rate of an early-type star. The UV resonance lines are by far the best indicators of v_∞, and the shape of the profile also provides good constraints on the gradient of the radial velocity field of the wind. Unfortunately, the strength of UV resonance lines cannot be converted to $\dot{M}$ easily because of the large uncertainties in the ionization balance of hot-star winds, uncertainties that are in part due to the presence of time-dependent processes in the wind. However, once v_∞ is known, continuum methods come to the fore, and measurements in the radio range between 1 mm and 20 cm are generally believed to provide the most reliable estimates of $\dot{M}$. In practice, though, the weakness of the flux levels due to free-free emission in hot-star winds limits the applicability of these techniques to the nearest objects, which nevertheless play a key role by acting as calibrators for other techniques.

In contrast, Hα emission profiles can now be observed with good spectral resolution for stars as far away as the Local Group of galaxies. Sufficiently strong emission permits estimates of the velocity gradient and $\dot{M}$, and some-

times also v_∞ (e.g., for late B and early A supergiants). The caveat applicable to these (and other) ρ^2 diagnostics is that they are very susceptible to the distribution of wind material assumed by the model used to interpret them. In particular, $\dot{M}$ will be systematically overestimated if a smooth, spherically symmetric model is used to interpret recombination line profiles from a wind that is in fact asymmetric or otherwise structured. More detailed physical information concerning the effect of rotation on the distribution of material in hot-star winds and the nature of the structures responsible for their ubiquitous variability is required in order to quantify this effect. There may still be uncertainties as large as a factor of two lurking in the determinations of the mass-loss rates of early-type stars.

Even so, the stationary properties of hot-star winds can be explained acceptably well by the theory of line-driven winds; see, e.g., the lectures by Lamers (this volume). Consequently, it seems likely that in the coming years stellar wind research will begin to emphasize the role these outflows can play as tools to investigate astrophysical problems. For example, Kudritzki and his colleagues are currently developing the "Wind-Momentum-Luminosity Relationship", by which the stellar wind profiles observed in the luminous stars of external galaxies can be used as "standard candles" to determine distances out to the Fornax and Virgo Clusters; see Kudritzki (1997) for details of this exciting application of stellar wind theory. More generally, stellar winds can be used to probe astronomical situations that range from the formation of bow shocks, bubbles, and chimneys in the interstellar medium to measuring the abundance gradients in external galaxies and determining the chemical composition of early generations of massive stars in high redshift galaxies. Observations of these phenomena represent the frontiers of stellar wind research; together with ongoing investigations into the nonstationary behaviour of hot-star winds, they are expected to provide further surprising insights into the physics of hot stars and their environments.

Acknowledgements

It is a pleasure to thank the organizers and participants of this summer school for many stimulating discussions concerning stellar atmospheres and astrophysics, and for the opportunity to sample a wide variety of Belgian beer – which is very compelling, despite the "impurities" that my Bavarian colleagues warned me about! I am indebted to Joachim Puls, Achim Feldmeier, Paco Najarro, Peter Petrenz, and Anne Fullerton for their contributions to this manuscript, and would like to express my thanks to the many colleagues around the world who have taught me about hot-star winds over the years, most particularly Stan Owocki and Joachim Puls. I would also like to thank Prof. R.-P. Kudritzki for the opportunity to deliver these lectures. Financial support from the Deutsche Forschungsgemeinschaft (grant Pu 117/3–1) during the preparation of the written version of these lectures is gratefully

acknowledged.

References

Abbott D. C., Bieging J. H., Churchwell E., Cassinelli J. P. (1980): ApJ **238**, 196
Abbott D. C., Bieging J. H., Churchwell E. (1981): ApJ **250**, 645
Abbott D. C., Bieging J. H., Churchwell E. (1984): ApJ **280**, 671
Abbott D. C., Bieging J. H., Churchwell E., Torres A. V. (1986): ApJ **303**, 239
Abbott D. C., Telesco C. M., Wolff S. C. (1984): ApJ **279**, 225
Altenhoff W. J., Thum C., Wendker H. J. (1994): A&A **281**, 161
Barlow M. J., Cohen M. (1977): ApJ **213**, 737
Beals C. S. (1930): Publ. DAO **4**, 271
Beals C. S. (1950): Publ. DAO **9**, 1
Bieging J. H., Abbott D. C., Churchwell E. (1982): ApJ **263**, 207
Bieging J. H., Abbott D. C., Churchwell E. (1989): ApJ **340**, 518
Bjorkman J. E., Cassinelli J. P. (1993): ApJ **409**, 429
Bjorkman J. E., Ignace R., Tripp T. M., Cassinelli J. P. (1994): ApJ **435**, 416
Carlberg R. G. (1980): ApJ **241**, 1131
Caroff L. J., Noerdlinger P. D., Scargle J. D. (1972): ApJ **176**, 439
Castor J. I. (1970): MNRAS **149**, 111
Castor J. I., Lamers H. J. G. L. M. (1979): ApJS **39**, 481
Chen W., White R. L., Bertsch D. (1996): A&AS **120**, 423
Contreras M. E., Rodríguez L. F., Gómez Y., Velázquez, A. (1996): ApJ **469**, 329
Cranmer S. R. (1996): Ph.D. thesis, Univ. of Delaware
Cranmer S. R., Owocki S. P. (1996): ApJ **462**, 469
Feldmeier A. (1995): A&A **299**, 523
Fullerton A. W., Gies D. R., Bolton C. T. (1992): ApJ **390**, 650
Gabler R., Gabler A., Kudritzki R. P., Puls J., Pauldrach A. W. A. (1989): A&A **226**, 162
Groenewegen M. A. T., Lamers H. J. G. L. M. (1989): A&AS **79**, 359
Groenewegen M. A. T., Lamers H. J. G. L. M. (1991): A&A **243** 429
Hamann W.-R. (1981): A&A **93**, 353
Hanson M. M., Conti P. S., Rieke M. J. (1996): ApJS **107**, 281
Hanson M. M., Geballe T. R., Conti P. S., Block D. L. (1993): A&A **273**, L44
Haser S. M. (1995): Ph.D. thesis, Ludwig-Maximilians-Universität München
Haser S. M., Lennon D. J., Kudritzki R.-P., Puls J., Pauldrach A. W. A., Bianchi L., Hutchings J. B. (1995): A&A **295**, 136
Henrichs H. F., Kaper L., Nichols J. S. (1994): A&A **285**, 565
Howarth I. D., Prinja R. K. (1989): ApJS **69**, 527
Howarth I. D., Prinja R. K., Massa D. (1995): ApJ **452**, L65
Hutchings J. B. (1979): *The O Stars: Optical Review,* in Mass Loss and Evolution of O-Type Stars (proceedings of IAU Symp. 83), ed. P. S. Conti & C. W. H. de Loore (Reidel, Dordrecht), p. 3
Ignace R., Cassinelli J. P., Bjorkman J. E. (1996): ApJ **459**, 671
Kaper L., Henrichs H. F., Nichols J. S., Snoek L. C., Volten H., Zwarthoed G. A. A. (1996): A&AS **116**, 257
Kaufer A., et al. (1997): A&A **320**, 273
de Koter A., Schmutz W., Lamers H. J. G. L. M. (1993): A&A **277**, 561

Kudritzki R. P. (1988): *The Atmospheres of Hot Stars: Modern Theory and Observation*, in Radiation in Moving Gaseous Media (18th Advanced Course of the Swiss Society of Astronomy & Astrophysics), ed. Y. Chmielewski & T. Lanz (Geneva: Geneva Observatory), p. 1
Kudritzki R. P. (1992): A&A **266**, 395
Kudritzki R.-P. (1997): *Quantitative Spectroscopy of the Brightest Blue Supergiant Stars in Galaxies*, in Stellar Astrophysics for the Local Group (Proceedings of VIII Canary Islands Winter School of Astrophysics), ed. A. Aparicio, A. Herrero, & F. Sánchez (Cambridge: CUP), in press
Kudritzki R. P., Hummer D. G. (1990): ARA&A **28**, 303
Lamers H. J. G. L. M., Cerruti-Sola M., Perinotto M. (1987): ApJ **314**, 726
Lamers H. J. G. L. M., Gathier R., Snow T. P. (1982): ApJ **258**, 186
Lamers H. J. G. L. M., Leitherer C. (1993): ApJ **412**, 771
Lamers H. J. G. L. M., et al. (1996): A&A **315**, 229
Lamers H. J. G. L. M., Waters L. B. F. M., Wesselius P. R. (1984): A&A **134**, L17
Lamers H. J. G. L. M., Waters L. B. F. M. (1984): A&A **136**, 37
Leitherer C., Chapman J. M., Koribalski B. (1995): ApJ **450**, 289
Leitherer C., Robert C. (1991): ApJ **377**, 629
Lucy L. B. (1971): ApJ **163**, 95
Lucy L. B. (1982): ApJ **255**, 278
Lucy L. B. (1983): ApJ **274**, 372
Lucy L. B., Solomon P. M. (1970): ApJ **159**, 879
MacGregor K. B., Hartmann L., Raymond J. C. (1979): ApJ **231**, 514
Maeder A., Conti P. S. (1994): ARA&A **32**, 227
Massa D., et al. (1995a): ApJ **452**, L53
Massa D., Prinja R. K., Fullerton A. W. (1995b): ApJ **452**, 842
Massa D., Shore S. N., Wynne D. (1992): A&A **264**, 169
Mihalas D. (1978): *Stellar Atmospheres* (Freeman, San Francisco)
Mihalas D. (1979): MNRAS **189**, 671
Mihalas D., Hummer D. G. (1973): ApJ **179**, 827
Moffat A. F. J., Drissen L., Lamontagne R., Robert C. (1988): ApJ **334**, 1038
Morrell N. I., Walborn N. R., Fitzpatrick E. L. (1991): PASP **103**, 341
Morton D. C. (1967a): ApJ **147**, 1017
Morton D. C. (1967b): ApJ **150**, 535
Morton D. C. (1976): ApJ **203**, 386
Mullan D. J. (1984): ApJ **283**, 303
Najarro F., et al. (1994): A&A **285**, 573
Olson G. L. (1982): ApJ **255**, 267
Owocki S. P. (1990): Reviews of Modern Astronomy **3** (Springer, Berlin), 98
Owocki S. P. (1992): *Instabilities in Hot-Star Winds: Basic Physics and Recent Developments*, in Atmospheres of Early-Type Stars, ed. U. Heber & S. Jeffery (Springer, Berlin), p. 393
Owocki S. P., Castor J. I., Rybicki G. B. (1988): ApJ **335**, 914
Owocki S. P., Fullerton A. W., Puls J. (1994): Ap&SS **221**, 437
Owocki S. P., Rybicki G. B. (1984): ApJ **284**, 337
Panagia N., Felli M. (1975): A&A **39**, 1
Pauldrach A. W. A., Kudritzki R. P., Puls J., Butler K., Hunsinger J. (1994): A&A **283**, 525

Pauldrach A. W. A., Puls J., Kudritzki R. P. (1986): A&A **164**, 86
Petrenz P., Puls J. (1996): A&A **312**, 195
Phillips R. B., Titus M. A. (1990): ApJ **359**, L15
Prinja R. K. (1988): MNRAS **231**, 21P
Prinja R. K., Fullerton A. W. (1994): ApJ **426**, 345
Prinja R. K., Howarth I. D. (1986): ApJS **61**, 357
Prinja R. K., Howarth I. D., Henrichs H. F. (1987): ApJ **317**, 389
Prinja R. K., Massa D., Fullerton A. W. (1995): ApJ **452**, L61
Prinja R. K., Massa D., Fullerton A. W., Howarth I. D., Pontefract M. (1997): A&A **318**, 157
Prinja R. K., Smith L. J. (1992): A&A **266**, 377
Puls J., Feldmeier A., Springmann U. W. E., Owocki S. P., Fullerton A. W. (1994): Ap&SS **221**, 409
Puls J., et al. (1996): A&A **305**, 171
Puls J., Owocki S. P., Fullerton A. W. (1993): A&A **279**, 457
Rivinius Th., et al. (1997): A&A **318**, 819
Runacres M. C., Blomme R. (1996): A&A **309**, 544
Rybicki G. B. (1984): *Escape Probability Methods*, in Methods of Radiative Transfer, ed. W. Kalkofen (Cambridge: CUP), p. 21
Rybicki G. B., Hummer D. G. (1978): ApJ **219**, 654
Rybicki G. B., Lightman A. P. (1979): *Radiative Processes in Astrophysics* (Wiley, New York)
Santolaya-Rey A. E., Puls J., Herrero A. (1997): A&A, in press
Schaerer D., Schmutz W. (1994): A&A **288**, 231
Snow T. P., Lamers H. J. G. L. M., Lindholm D. M., Odell A. P. (1994): ApJS **95**, 163
Stahl O., et al. (1993): A&AS **99**, 167
Underhill A. B. (1958): Mem. R. Soc. Liège **20**, 91
Underhill A. B. (1995a): ApJS **100**, 433
Underhill A. B. (1995b): ApJS **100**, 461
Vallée J. P., Moffat A. F. J. (1985): AJ **90**, 315
Walborn N. R., Bohlin R. C. (1996): PASP **108**, 477
Walborn N. R., Nichols-Bohlin J. S., Panek R. J. (1985): International Ultraviolet Explorer Atlas of O-Type Spectra from 1200 to 1900 Å (NASA RP–1155)
Walborn N. R., Parker J. W., Nichols J. S. (1995): International Ultraviolet Explorer Atlas of B-Type Spectra from 1200 to 1900 Å (NASA RP–1363)
White R. L. (1985): ApJ **289**, 698
White R. L., Becker R. H. (1982): ApJ **262**, 657
White R. L., Becker R. H. (1983): ApJ **272**, L19
Wilson R. (1958): Mem. R. Soc. Liège **20**, 85
Wolf C. J. E., Rayet G. (1867): Observatoire de Paris Comptes Rendus **65**, 292
Wright A. E., Barlow M. J. (1975): MNRAS **170**, 41